

Elimination of Artificial Grid Distortion and Hourglass-Type Motions by Means of Lagrangian Subzonal Masses and Pressures

E. J. Caramana and M. J. Shashkov

Hydrodynamics Methods Group MS-D413, Mathematical Modelling and Analysis Group MS-B284, Applied Theoretical and Computational Physics Division, Theoretical Division, Los Alamos National Laboratory, Los Alamos, New Mexico 87545

Received May 13, 1997; revised February 5, 1998

The bane of Lagrangian hydrodynamics calculations is the premature breakdown of grid topology that results in severe degradation of accuracy and run termination often long before the assumption of a Lagrangian zonal mass has ceased to be valid. At short spatial grid scales this is usually referred to by the terms “hourglass” mode or “keystone” motion associated, in particular, with underconstrained grids such as quadrilaterals and hexahedrons in two and three dimensions, respectively. At longer spatial lengths relative to the grid spacing there is what is referred to ubiquitously as “spurious vorticity,” or the long-thin zone problem. In both cases the result is anomalous grid distortion and tangling that has nothing to do with the actual solution, as would be the case for turbulent flow. In this work we show how such motions can be eliminated by the proper use of subzonal Lagrangian masses, and associated densities and pressures. These subzonal pressures give rise to forces that resist these spurious motions. The pressure is no longer a constant in a zone; it now accurately reflects the density gradients that can occur within a zone due to its differential distortion. Subzonal Lagrangian masses can be chosen in more than one manner to obtain subzonal density and pressure variation. However, these masses arise in a natural way from the intersection of the Lagrangian contours, through which no mass flows, that are associated with both the Lagrangian zonal and nodal masses in a staggered spatial grid hydrodynamics formulation. This is an extension of the usual Lagrangian assumption that is often applied to only the zonal mass. We show that with a proper discretization of the subzonal forces resulting from subzonal pressures, hourglass motion and spurious vorticity can be eliminated for a very large range of problems. © 1998 Academic Press

The U.S. Government’s right to retain a nonexclusive royalty-free license in and to the copyright covering this paper, for governmental purposes, is acknowledged.

1. INTRODUCTION AND STATEMENT OF PROBLEM

Lagrangian hydrodynamics algorithms have been in wide use for perhaps the longest time of any numerical methods employed for the solution of complex problems of fluid flow [1]. The major assumption of all of these algorithms is that one can define a mass element inside a zone such that, although the zone changes its shape as its vertices move in time, no mass crosses its boundaries. Thus the mass element is “tracked” in time. Newton’s laws of motion are most naturally written in Lagrangian form when applied to point masses or rigid bodies. The Lagrangian zone mass concept can be viewed as an extension of this notion when considered with respect to a staggered grid in space where intensive variables such as density, pressure, and specific internal energy are defined in a zone, and coordinate position and velocity are located at the points or vertices, usually connected by straight lines, that define the circumscribed zones. It is these kinds of schemes that we will be concerned with here, although conceptually simpler Lagrangian algorithms where all variables are point-centered have also been widely investigated. In this paper we will extend the idea of a Lagrangian zone mass to remove the numerical difficulties that we refer to loosely as “anomalous grid distortion” that have plagued these methods since their inception.

The Lagrangian assumption of a constant zonal mass is valid for problems that might best be described as compressible, deterministic flow where mixing instabilities and turbulence are not fully developed. These methods are very useful when a high resolution of interfaces and other sharp discontinuities is desired. For strictly incompressible flow the assumption of a Lagrangian zonal mass breaks down rapidly. However, both Eulerian and ALE (arbitrary Lagrangian–Eulerian) codes developed specifically to simulate these kinds of problems often employ a splitting method whereby the “physics” is computed by a separate Lagrangian step. Then the kinematical questions of grid point location and the fluxing of variables to new zones and points is dealt with separately. Since we are concerned with the Lagrangian step of this procedure, the results given here are germane to these algorithms.

The anomalous grid distortion that we are concerned with can be placed into two broad categories. The first of these contains the hourglass modes that appear as a global mesh distortion at the shortest spatial grid scale. They were first noted in the work by Maenchen and Sack [2]. These motions result because a quadrilateral or hexahedral grid in two or three dimensions, respectively, is underconstrained with respect to the total number of degrees of freedom of the grid [3, 4]. The second type of anomalous grid distortion occurs at larger spatial scale with respect to the grid spacing. This is referred to as spurious vorticity by Dukowicz and Meltz [5], and as the long-thin zone problem by Browne and Wallick [6]. Although often present in calculations, these difficulties are really only precisely definable with respect to known one-dimensional solutions using grids that are skewed in some manner with respect to an ignorable coordinate in two or more dimensions. Here the solution gradients are misaligned with the coordinate grid. This can then give rise to vorticity that is completely absent from the known solution. The basic problem of anomalous grid distortion can be best illustrated in terms of the hourglass difficulty that is explained next.

Consider the six patterns of motion illustrated in Fig. 1 that are depicted in terms of a single quadrilateral zone where the arrows indicate the velocity vector at the grid points. It is possible to repeat any of these six patterns globally across the entire grid. They define the six global physical motions of the grid in two dimensions: two each of translation, extension (contraction), and shear. (Note that a pure rotation can be obtained by subtracting two patterns of shear in orthogonal directions.) A single quadrilateral has eight degrees of

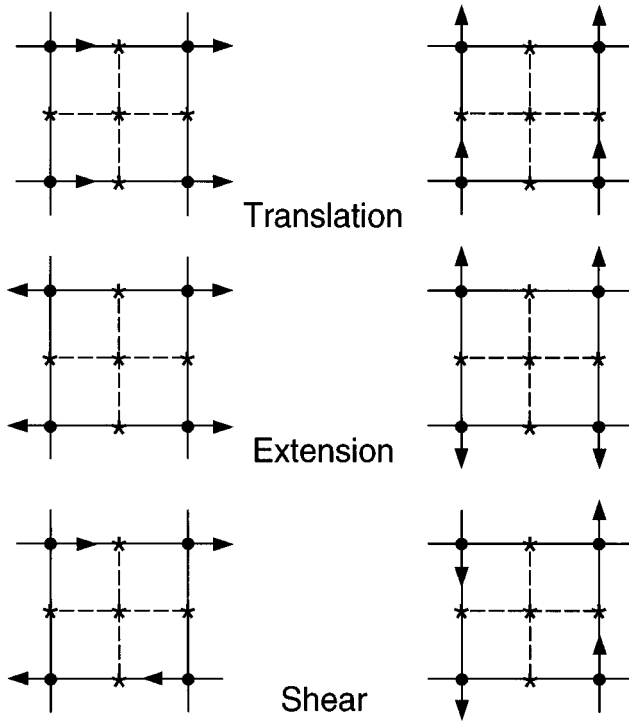


FIG. 1. Global physical modes of a quadrilateral grid.

freedom corresponding to the two independent directions of each of its four defining points. However, only the six global patterns shown in Fig. 1 are physical; an additional two patterns are the unphysical hourglass motions in each independent direction that are also global across the grid. For this reason quadrilateral grids are referred to as “underconstrained” [3, 4].

A pure hourglass motion in two dimensions consists of a checkerboard pattern with a velocity field in a given direction that alternates in sign at every grid point, as shown in Fig. 2.

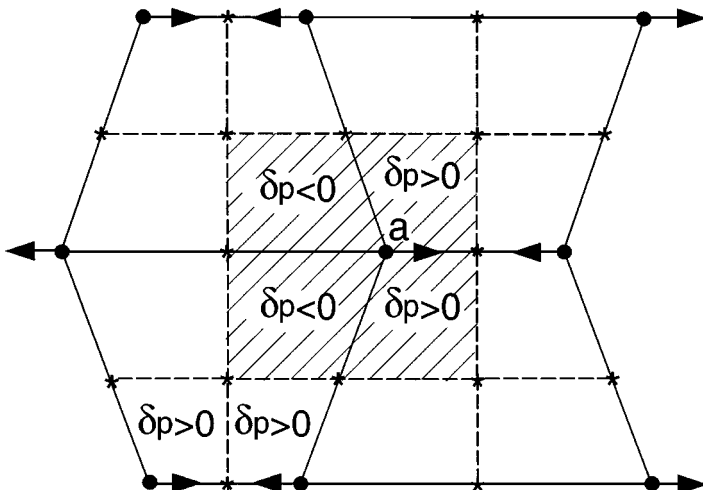


FIG. 2. Hourglass pattern of zones about point a ; dashed lines indicate median mesh.

There is one such pattern in each direction for a two-dimensional quadrilateral grid. In three dimensions there are more such patterns associated with hexahedral grids [4]. In Fig. 2 the zones are constructed from dynamical grid points shown as solid dots that are connected by solid lines with associated arrows indicating the direction of the velocity field, which alternates sign from point to point. Shown as dashed lines is the so-called median mesh that connects midpoints of sides to zone centers. These points are defined by coordinates and velocities that are simple averages (one-half or one-quarter) of those of the points that define the zone.

Let us next consider how the dynamical equations respond to the eight global patterns of motion of a staggered spatial grid composed of quadrilateral zones. To obtain a dynamical response to some motion the equations for force and internal energy must exhibit a reaction to the motion. In Lagrangian form the equations for acceleration from a force due to a pressure p , and for the evolution of the specific internal energy e , are given as

$$\rho \frac{d\mathbf{v}}{dt} = -\nabla p, \quad (1)$$

$$\rho \frac{de}{dt} = -p \nabla \cdot \mathbf{v}, \quad (2)$$

where the pressure is obtained from an equation of state, $p = p(e, \rho)$. If the volume of a zone does not change, its density is constant, and also, the specific internal energy does not change since in this case $\nabla \cdot \mathbf{v} = 0$. This latter result follows from the equation for the continuity of mass written in Lagrangian form: for $\rho = M_z / V_z$, where M_z is the constant mass of a zone with volume V_z , this is

$$\nabla \cdot \mathbf{v} = \frac{1}{V_z} \frac{dV_z}{dt}. \quad (3)$$

Of the eight global motions that have been enumerated it is thus seen that only the ones corresponding to extension (contraction) elicit a direct response from the dynamical equations independently of the boundary conditions; the others leave the volume of the quadrilateral zone unchanged. However, both the shear and translation patterns are physical and cause no difficulties. The difficulty is with the unphysical hourglass patterns. They are generally found to grow with time at a rate that is not easy to predict.

A possible solution to this problem that has long been recognized is to allow for subzonal volumes, Lagrangian masses, and thus, subzonal densities and pressures that produce subzonal forces, since the root of the difficulty is that the zone volume does not change in response to hourglass motion. Focus on point a as shown in Fig. 2. If we consider the four subvolumes shown as hatched regions that all contain point a as a vertex, then these subvolumes do change as it moves, as can be seen from this figure. If we consider the masses inside these subzonal volumes to be constant, Lagrangian objects in addition to the total mass of a zone, then from these changing subvolumes separate densities, and thus pressures, can be computed. If we measure as δp the difference of the pressure in these subzones and the unchanged mean zone pressure, then we obtain qualitative values of δp about point a as shown in Fig. 2. These pressures produce forces that obviously oppose its motion and also that of the hourglass pattern everywhere across the grid. At the same time it is important to note that they provide no resistance to the physical patterns of either translation or shear. For extension (contraction) both the zone and subzone volumes change. In this case the values

of δp that are obtained are the same as those that are found from subtracting the pressures that result from refining the grid by a factor of two in each direction from the zone pressure of the unrefined grid. Thus, these subzonal pressures do not oppose this physical motion.

The major aim of this paper is to develop the consequences of the inclusion of subzonal forces into otherwise standard Lagrangian algorithms. To this end the following issues must be considered: the choice of and justification for subzonal Lagrangian masses, the proper dynamical treatment of the subzonal forces that arise from them, their efficacy on relevant test problems including limitations with regard to possible anomalous grid stiffening, and also, their effectiveness in counteracting the spurious vorticity, or long-thin zone problem, that is not as straightforwardly defined as is hourglass motion.

The organization of the rest of this paper is as follows: In the next section we briefly review previous work on this subject. This essentially consists of two different approaches: filters, where the unphysical motion is detected and removed kinematically; and, dynamical approaches such as subzonal Lagrangian masses and associated pressures, which is the procedure that we generalize, and certain forms of artificial viscosity that respond to hourglass motion and spurious vorticity. The framework in which we perform control volume discretizations of the equations is briefly discussed in Section 3. Here is introduced the concept of “compatibility” that allows us to compute the correct change of internal energy that arises from subzonal forces. In Section 4 we define the subzonal Lagrangian masses that we will use in this study. These are either quadrilaterals or triangles in two dimensions. Section 5 gives the manner in which the force calculated from the subzonal pressures is to be utilized to move the dynamical grid points. We treat the subzonal pressure as a perturbation and employ a separate force calculation from that used for the mean pressure of the zone. Here we introduce the concept of nondynamical points. These are points that have forces associated with them but have velocities that are computed as averages of those of the dynamical points whose evolution is determined by the momentum equation. This force differencing is not unique since the force that is exerted on a dynamical point from an adjacent zone becomes dependent on the path of integration taken through the zone when the zone pressure is no longer a constant. This leads to the definition of a “merit factor” to multiply the strength of these forces. This is not unlike the choice of coefficients in the treatment of artificial viscosity. The important concern is to show that such coefficients, although somewhat case dependent, have a wide enough dynamic range so that the class of problems that can be computed using this technique are not limited to a narrow set. How this merit factor can be easily automated is also considered. In Section 6 we discuss the problem of the choice of grid elements in two dimensions. This question is: Under what conditions are triangles artificially “stiff” for compressible flow problems? Quadrilaterals tend to be artificially “floppy.” Finally, in Section 7 a range of numerical results is presented to show the effectiveness of our treatment both with respect to previously published work and with respect to the sensitivity of the merit factor that we have introduced into this formulation. We close with a brief summary of our conclusions.

2. PREVIOUS WORK

Here we discuss the general types of spurious vorticity treatments that have been utilized to attack this problem. For high spatial frequency hourglass motions, filters have been devised that detect and separate the spurious motion from the mean physical velocity field [3, 4]. The problem with this approach is that the patterns that are sought are global across

the grid while the filters that have been devised to detect them are usually based on local samplings of the velocity field. If there is a large spatial scale separation between the high-frequency spurious, and low-frequency physical, velocity field, then to lowest order the spurious velocity field carries no kinetic energy and the filtering approach can be very effective. If this is not the case the filters will pollute the physical velocity field, particularly if the underlying grid is not regular. Then total energy will not be conserved unless the modified nodal kinetic energy is converted into internal energy of the zones. However, since the filtering approach is usually kinematical with no forces directly computed, energy conservation can only be achieved on an ad hoc basis.

An approach that has been employed with high speed flow problems is to utilize an artificial viscosity that is edge-centered [7], that is, consists of a separate discrete artificial viscosity term with respect to each edge of a zone. These separate viscosity terms also respond to hourglass patterns and spurious vorticity; they can turn on whenever an edge of a zone is under compression (one must set an appropriate condition for this). They thus provide some resistance to these motions [8]. However, it is not always clear to what degree they artificially damp the physical solution. We also employ an edge-centered viscosity that utilizes advection-type limiters that reduce its effect in regions where strong shock disturbances are not present [9]. The question of the use of artificial viscosity to maintain grid integrity versus our subzonal pressure approach will be addressed in Section 7 when we consider numerical examples.

Another approach is to subdivide a quadrilateral mesh into four triangular subzones whose masses are taken to be Lagrangian. In the temporary triangular subzoning (TTS) treatment [6] not only is this done, but the work due to both pressure and artificial viscosity forces is also deposited in the triangular subzone volumes. Then a pressure is calculated for this subzone that is used to compute the acceleration of its two adjacent nodal points. At the end of each timestep the internal energy is averaged across the zone to give a mean value for the start of the next timestep. This is performed without reference to any characteristic timescale, and thus has no physical justification. In a modified form known as soft-TTS [6] the density in the triangles is relaxed toward the zone average using a timescale determined by the quadrilateral length scales divided by the zone sound speed. A variant of the TTS procedure wherein the specific internal energy is always taken to be constant within a zone has been pursued by Burton [10]. Here also, triangles are used as the subzones, and in some cases the density is relaxed with time throughout the zone.

Work by Goloviznin *et al.* [11] parallels the TTS approach to a degree but is somewhat more general. They construct an arbitrary number of Lagrangian subzonal entities that can be either triangular or quadrilateral with respect to a grid with quadrilateral zones. These subzones are then constrained to have the same specific internal energy, but with different densities because of their separate volumes and constant, Lagrangian masses. Although an arbitrary number of subzones can be constructed in a given quadrilateral only a small number are utilized in practice. The general procedure that we employ to define the auxiliary points used in constructing any such subzones, their associated forces, and how they are utilized in a force calculation is discussed in Section 5. That employed by Goloviznin and co-workers can be viewed as a subset of the line of reasoning given in that section.

The procedure employed by Dukowicz and Meltz [5] is very specialized. They evolve a separate equation for the vorticity in addition to the usual velocity field. The “correct” velocity field must then be reconstructed on every timestep from its proper divergence and vorticity, utilizing appropriate boundary conditions. There is related work by Burton that

is termed “spurious excess vorticity damping” [12]. In this method a “true” vorticity is calculated on the basis of the curl of the velocity field computed with respect to the zone centers in a staggered grid formulation. The curl of the velocity field computed with respect to an edge is then compared to these zone values. Based on the discrepancy of the two quantities forces are calculated and used in the momentum equation to drive this difference to zero. Although a “spurious” component of the velocity field is deduced as in the filter approach, this scheme will automatically preserve momentum and energy and is much less costly than that of Dukowicz and Meltz. The main difficulty with all of these methods is how to decide what part of the velocity field is spurious and what part is not.

Finally, one can simply utilize triangles as grid elements in two dimensions. Although there is no hourglass motion associated with these elements in a staggered spatial grid formulation, this introduces additional difficulties. The most important of these is the artificial stiffness of triangular elements for certain flow conditions. This is discussed in Section 6 since it impacts the choice of subzonal masses that one declares to be Lagrangian. Also, the use of triangular zones does not address the spurious vorticity issue still present at length scales larger than the grid spacing.

3. COMPATIBLE DISCRETIZATION

In order to establish the framework used in the rest of our development we consider in discrete form the conservation of total energy, the momentum equation, and the internal energy equation. Our purpose is to present a brief summary of what is known as the “compatible” discretization of these equations that is valid for a staggered spatial placement of variables [13]. In this discretization the three mentioned equations are differenced such that if the discrete form of any two are specified the third results as an algebraic identity. Thus, once one specifies a discrete form for conservation of total energy and the equation for internal energy, the discrete form of the momentum equation follows automatically. In a completely reciprocal manner the discrete form of conservation of total energy and the momentum equation can be specified, and the discrete version of the internal energy equation results. This procedure is equivalent to specifying in discrete form a vector differential operator (say the divergence that is used to compute volume changes in the internal energy equation) from which the conjugate operator (the gradient used to compute force in the momentum equation) is then derived, or vice versa. When viewed in this way this is an example of the method of support operators [14, 15]. If the force in discrete form is specified in some manner that cannot necessarily be viewed as the direct discretization of the vector operators acting on a function, which is the case for some of the results given in Section 5 and for our particular form of artificial viscosity [9], then a compatible form of discretization is the only one that will allow us to compute in a systematic manner the rate of work done by these forces as needed for the complete specification of the internal energy equation. An additional benefit of a compatible formulation is that total energy is always conserved to roundoff error in discrete form. While the full discussion of compatibility is presented elsewhere [13], the minimum of results needed for the rest of our work is given next.

Conservation of total energy can be written as

$$\sum_z M_z e_z + \sum_p M_p \mathbf{v}_p^2 / 2 = \text{Boundary Work}, \quad (4)$$

where e_z is the specific internal energy and M_z is the mass in zone z , M_p is the mass associated with the point or node p , and \mathbf{v}_p is the grid point velocity. Thus the internal and kinetic energies are defined in the zones and at the grid points, respectively. We can without loss of generality neglect the boundary work term in Eq. (4) and take its time variation to obtain

$$\sum_z M_z \delta e_z + \sum_p M_p \mathbf{v}_p \cdot \delta \mathbf{v}_p = 0. \quad (5)$$

Here δ denotes the change of a quantity in a discrete time increment. Note that in obtaining Eq. (5) from Eq. (4) we have considered both zone and node masses to be constant.

The force equation at point p can be written as

$$M_p \frac{d\mathbf{v}_p}{dt} = \mathbf{F}_p \equiv \sum_z \mathbf{f}_z^p. \quad (6)$$

In this equation we have defined a new object, \mathbf{f}_z^p , that we call the corner force. This force acts from zone z and is applied to point p such that if one sums all corner forces common to this point, and that also belong to the neighboring zones that contain this point as a vertex, then the total force acting on point p , \mathbf{F}_p , is obtained. The corner force is thus defined with two indicies: one that refers to the zone in which it is constructed, and one indicating the point onto which it acts. In our notation, $\mathbf{f}_z^p = \mathbf{f}_p^z$, except that we always sum this object with respect to the lower index. The explicit functional form of the corner force is, as yet, undefined. How this may be defined for forces arising from subzonal pressures is given in Section 5, and is the major topic of this paper.

The rate of work done by corner forces of any functional form, and thus, the change in internal energy due to them can be computed “compatibly” utilizing conservation of total energy. The main point is that the rate of exchange of kinetic energy from gridpoint p to zone z due to the corner force \mathbf{f}_z^p is simply the dot product of this force into the velocity of gridpoint p . (This can be rigorously justified [13].) Then it follows from Eqs. (5), (6) after performing a discrete change of summation by parts that, in general, the change in internal energy produced by any corner force, \mathbf{f}_p^z , can be generically calculated by

$$\delta e_z = - \frac{\sum_p \mathbf{f}_p^z \cdot \mathbf{v}_p \Delta t}{M_z}, \quad (7)$$

where δe_z is the change of the specific internal energy of a zone in a time Δt . It is Eqs. (4), (6), (7) that constitute an algebraic identity for an arbitrary form of the corner force object \mathbf{f}_z^p .

Next, as an example, we give a realization of \mathbf{f}_z^p for a pressure p_z that is constant in a zone using control volume differencing. Shown in Fig. 3 are the eight half-edge vectors \mathbf{a}_i that have the direction of the outward normal to the sides of the quadrilateral z and magnitudes equal to one-half of the length (area) of their respective sides. From these vectors the corner force associated with the zone z and the point p with respect to the mean zone pressure p_z is simply given as $\mathbf{f}_z^p \equiv p_z (\mathbf{a}_2 + \mathbf{a}_3)$. That is, this force acts from zone z and is applied to point p due to the pressure p_z . This is the basic form of the usual control volume differencing that we utilize in the rest of this work [16, 13]. If the sum indicated in Eq. (7) is computed analytically, then the result is found to be equivalent to $-p_z dV_z/M_z$ [13], where dV_z is the

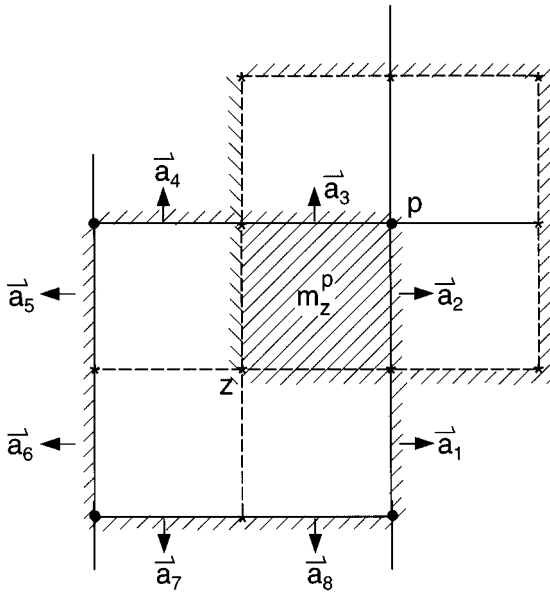


FIG. 3. Quadrilateral zone and median mesh for defining corner mass m_z^p . Hatched lines denote Lagrangian boundaries of coordinate-line (solid) and median (dashed) mesh. \vec{a}_i are outward normals to coordinate-line mesh.

discretized functional form of the change in volume of zone z in a timestep; and thus, this yields the usual result.

In the remainder of this paper, in addition to the mean zone pressure p_z , we consider separate subzone pressures p_z^s that arise, through the equation of state, from the difference $\delta\rho$ between the subzone density and the zone density. We define $\delta p \equiv p_z^s - p_z$, and are concerned with constructing difference equations for the perturbed corner forces, denoted as $\delta\mathbf{f}_p^z$, associated with the perturbed pressures δp . (e_z is always constant in space for any given zone z .) In this case the change in internal energy due to these forces is always computed compatibly by inserting $\delta\mathbf{f}_p^z$ in place of \mathbf{f}_p^z in Eq. (7).

4. SUBZONAL LAGRANGIAN MASSES

We next define what is meant by Lagrangian subzonal masses. Although this discussion is given in terms of a quadrilateral grid in two dimensions, all of the arguments apply to any type of grid in any number of dimensions.

In Fig. 3 we show a quadrilateral zone labeled z and single out one of its defining points (vertices) and label it p . Aside from the grid points indicated by solid dots where the velocity is stored, we define with asterisks auxiliary points connected by dashed lines; the grid points are connected by solid lines. The coordinates of these auxiliary points are either zone centers or side midpoints of a given zone, as previously described. We refer to the solid lines that connect grid points as the coordinate-line mesh, while the dashed lines connecting the auxiliary points define the median mesh. The mass inside zone z , that we denote as M_z , is considered to be a constant in time with its initial value. The boundary of this zone is shown as a closed segment consisting of four straight lines of the coordinate-line mesh that is hatched to indicate that through this boundary no mass is allowed to flow. Similarly, we show about point p a closed boundary that consists of the median mesh connected

through the midpoints of sides and the zone centers about this point. Inside this boundary is contained the mass denoted as M_p that is associated with point p . This boundary is also shown as hatched indicating that no mass is allowed to flow through it. That is, in addition to the zone mass being constant we postulate that the point mass M_p is also a constant in time with its initial value. This is an extension of the usual Lagrangian assumption that is most often only applied to the zone masses. We now explore the consequences of this additional assumption.

The mass inside the hatched region in Fig. 3 is defined by the two side midpoints adjacent to point p , the center of the zone z , and the point p . This region is also defined by the intersection of median mesh and coordinate line boundaries through the aforementioned points. Since mass is not allowed to flow through either of these boundaries the mass inside this volume must also be a constant in time with its initial value. This volume we define as the quadrilateral subzone corner volume whose associated mass we label as m_p^z . We call this the corner mass associated with the zone index z and the grid point index p . So defined, the corner mass is always a quadrilateral in two dimensions regardless of the shape of the zone of which it is a part. Now we can proceed in the other direction and define the zonal mass M_z as the sum of all corner masses common to a zone, and the nodal mass M_p as the sum of all corner masses common to a grid point. This is given below as

$$M_z = \sum_p m_p^z, \quad M_p = \sum_z m_z^p. \quad (8)$$

As with our previous definition of corner forces, $m_p^z = m_z^p$, but summations always take place with respect to the lower subscript.

Note that one could equally well have declared the corner mass as defined above to be a constant, Lagrangian object and then the Lagrangian character of both the zonal and nodal mass follows from their definitions as given by Eq. (8). In most algorithms where the nodal mass is considered Lagrangian in addition to the zonal mass the consequences deduced by the explicit intersection of Lagrangian boundaries have been ignored. The subzonal densities arise from dividing these subzonal Lagrangian masses by their associated volumes.

In addition to considering the corner masses Lagrangian we will also treat the case where a quadrilateral is subdivided, using the zone center point and the pairs of points of each side, into four triangular masses that are considered to be Lagrangian. In this instance the zone and node masses are also Lagrangian from Eq. (8), where one-half of the mass of each of two triangular subzones contribute to each corner mass. The assumption of Lagrangian triangular subzonal masses is interesting for historical reasons since they have been used in the TTS context, also, because the subzonal forces associated with subtriangles are conceptually easier to investigate, and because the use of triangles versus quadrilaterals as grid elements is instructive to consider in this new context.

5. SUBZONAL FORCES/NONDYNAMICAL POINTS

Suppose that we integrate the fluid equations with higher order formulas such that we are given more than one value of the pressure inside a zone. Then using some choice of interpolant the pressure at every position inside the zone can be constructed, though this interpolation is not unique. Next we must decide on an integration path for computing the force through the zone that is due to pressure; this force is then applied to the dynamical points of this zone. One might use the median mesh with straight lines

connecting the side midpoints of the zone with the zone center point. However, this force will be different if this path of integration is curved in some manner. The force is path independent through a zone, and depends only on the path entry and exit points, only when the pressure is constant in the zone; this follows from the simple addition of vector lengths inside the zone all multiplied by the same common value of p_z . Thus we see that depending on the choice of interpolant, and the path of integration through the zone, different values of the force applied to a dynamical point will be obtained. Also, since these paths of integration are common to two adjacent points of a zone the force applied to one point will be equal in magnitude and opposite in direction to that applied to the other point. In this way Newton's third law is always obeyed and total momentum is conserved.

Instead of following the procedure outlined above we find it more transparent and physically motivated to utilize a different approach. In place of first choosing an interpolant to define the pressure throughout a zone we treat the difference in the subzonal pressure and the mean zone pressure as piecewise constant in subzonal volumes that are either triangles or quadrilaterals in two dimensions. Then the forces due to these piecewise constant perturbed pressures can be calculated along the boundaries of these subzones. They must all be accounted for with respect to the dynamical points. However, this can be done in more than one way consistent with momentum conservation and as a consequence the net force on the dynamical points from the same set of subzonal perturbed pressures can have different values depending on what choices are made. This entire procedure can be viewed as the equivalent of defining different interpolants and integration paths as noted above. However, to allow more flexibility we multiply the forces that result from a given choice by a nondimensional factor that can be used to connect the magnitudes of different discretizations that could have been made. This factor can also be allowed to vary on a zone basis consistent with momentum conservation. This we call the "merit factor." The force differencings that can be obtained by considering the subzonal perturbed pressures to be piecewise constant necessitates the introduction of the concept of nondynamical points, a topic we next address.

By nondynamical points we mean those points that have forces associated with them due to the presence of subzonal pressures but whose velocities are slaved as a simple average to the dynamical points that constitute the grid. Such a situation is shown in Fig. 4a where we show a quadrilateral zone with triangular subzones. Here the zone center point, labeled as number 5, is nondynamical in that its position and velocity are determined as one-quarter of the sum of the surrounding points. Our goal is to develop a procedure for treating the forces associated with nondynamical points. The first constraint in dealing with subzonal perturbed forces is conservation of momentum, which is now briefly considered in discrete form.

Conservation of momentum for a pressure that is constant in a zone takes on an extremely simple form. Conservation of momentum is the statement that the sum of all forces acting on all dynamical points be equal to the total applied boundary force. However, pressure exerts a force normal to all surfaces of a closed zone. From this fact it follows that conservation of momentum is true on a single zone basis. To see this consider the sum of the pressure forces taken by zones rather than by points. This yields

$$\sum_z \sum_{i=1}^8 \mathbf{f}_i^z = \sum_z \sum_{i=1}^8 p_z \mathbf{a}_i = \sum_z p_z \sum_{i=1}^8 \mathbf{a}_i = 0, \quad (9)$$

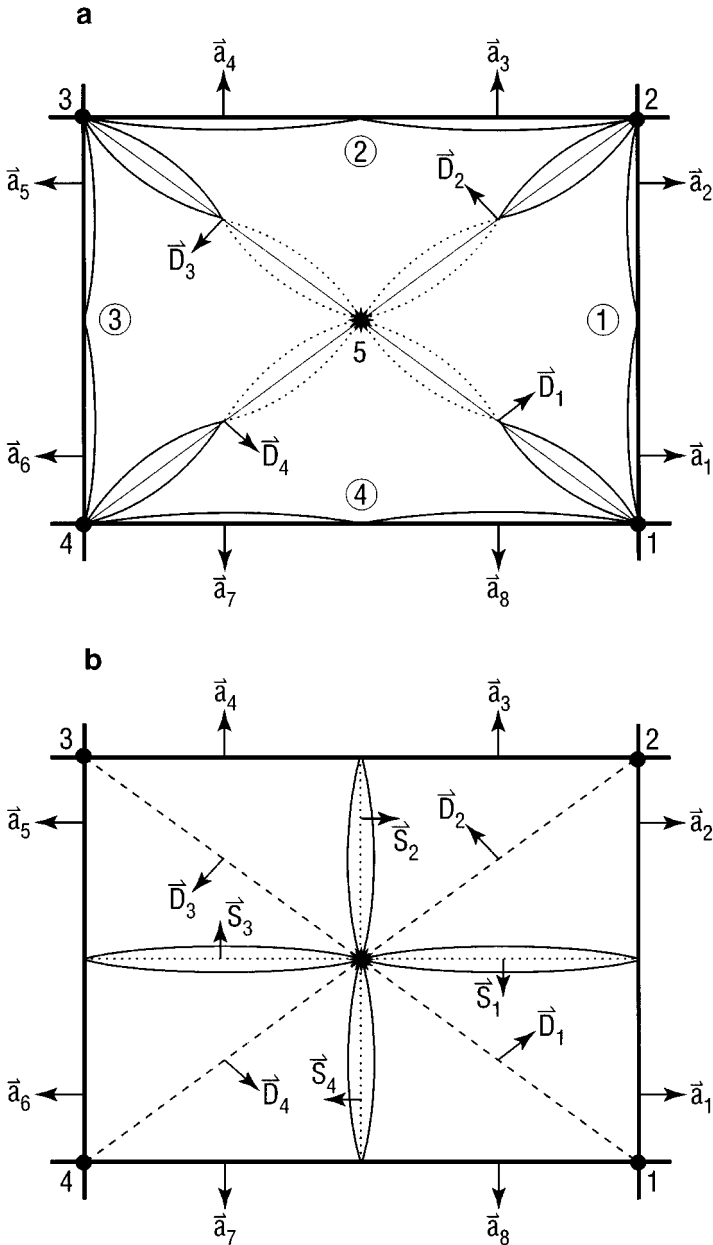


FIG. 4. (a) Quadrilateral zone: force contours for triangular subzonal forces differenced as Eqs. (11), (12). (b) Quadrilateral zone: force contours for triangular subzonal forces differenced as Eq. (14).

for the case when the boundary force vanishes and where vectors \mathbf{a}_i are the outward surface normals shown in Fig. 4a. Now, since p_z is arbitrary this equation can only be satisfied on a single zone basis. That this is true follows from the fact that the zone is closed, since the sum of the surface normals of any closed region is zero. Thus, conservation of momentum for a constant pressure in a zone is simply the topological statement that the zone is simply connected and closed. Since a single zone can be constructed as the sum of all of its subzones, the sum of all of the subzonal forces associated with subzonal

pressures, each constant in their respective subzones, must be equal to zero. We just need to account for all of them when distributing them among the dynamical points that make up the zone. Then their net momentum contribution is zero. This is the principal criterion that we use in dealing with subzonal forces. However, this does not yield a unique force differencing; the subzonal forces can be distributed among the dynamical points in many ways that are found to give different results, as previously discussed. This gives rise to the aforementioned “merit factor” that can be zone dependent and multiplies all subzonal forces of a given zone. Since momentum is conserved on a single zone basis this is still consistent with momentum conservation. This factor serves to connect the different strength effects of the force discretizations that we now develop. These are all based loosely on the idea that consistent with momentum conservation the subzonal forces should be distributed to the corner forces associated with the dynamical points in some unbiased, symmetrical manner.

We begin our discussion of how to distribute forces from nondynamical to dynamical points using the triangular subzones depicted in Fig. 4a. This figure shows eight vectors, \mathbf{a}_i , that are the outward half-edge normals to a quadrilateral zone. Although here each pair of half-edge vectors are equal, this is not always the case [17] and for the discussion that follows it is convenient to keep them separate. Inside we show four subtriangular zones labeled by the circled numbers one to four, and formed by four half-length diagonals whose normals are labeled \mathbf{D}_i , $i = 1 \cdots 4$. There we draw the force “contours” associated with the dynamical grid points labeled 1–4, as well as with the nondynamical center point 5. These force contours are shown as solid curves for the dynamical points and as dotted curves for the nondynamical center point. They are, of course, straight lines along the \mathbf{a}_i and \mathbf{D}_i vectors; they are shown as curves so that they can be distinctly seen. We will sometimes refer to the interior ones, such as along the half pieces of the interior zone grid vectors \mathbf{D}_i in Fig. 4a, as “force lobes.” We denote these forces by the vectors \mathbf{G}_i , $i = 1 \cdots 5$. For the grid point 1 and the nondynamical center point 5 these forces are given by

$$\mathbf{G}_1 = \delta p_1 \mathbf{a}_1 + \delta p_4 \mathbf{a}_8 + (\delta p_4 - \delta p_1) \mathbf{D}_1 / 2, \quad (10)$$

$$\mathbf{G}_5 = \frac{1}{2} [(\delta p_4 - \delta p_1) \mathbf{D}_1 + (\delta p_1 - \delta p_2) \mathbf{D}_2 + (\delta p_2 - \delta p_3) \mathbf{D}_3 + (\delta p_3 - \delta p_4) \mathbf{D}_4], \quad (11)$$

where δp_i is the perturbed subzonal pressure in the i th triangular subzone. The easiest way to find the perturbed corner forces, $\delta \mathbf{f}_{z,c}^p$, associated with the dynamical grid points of the quadrilateral is to add one-quarter of \mathbf{G}_5 to each of the forces \mathbf{G}_i that is already defined with respect to a dynamical grid point. Thus, our first form for these forces associated with zone z and point $p = 1$ is given by

$$\delta \mathbf{f}_{z,1st}^{p=1} = \mathbf{G}_1 + \frac{1}{4} \mathbf{G}_5. \quad (12)$$

The above gives a general prescription for finding the force discretization when nondynamical points are present: treat all points as dynamical and construct a proper force differencing; then distribute forces associated with the nondynamical points among the dynamical points with the same weight factors that are used to enslave the nondynamical points to the dynamical grid points.

Let us consider another possibility wherein the four force lobes that comprise \mathbf{G}_5 are simply added to their respective members along each diagonal. This gives a second form

for the perturbed corner forces, which at point $p = 1$ is

$$\delta \mathbf{f}_{z,2nd}^{p=1} = \mathbf{G}_1 + (\delta p_4 - \delta p_1) \mathbf{D}_1 / 2. \quad (13)$$

In Fig. 4b we show the vectors \mathbf{S}_i that are normals to the lines connecting the edge midpoints to the zone center point. These vectors define the median mesh. From this figure it is apparent that $\mathbf{S}_4 = -(\mathbf{D}_1 + \mathbf{a}_8)$ and $\mathbf{S}_1 = \mathbf{a}_1 - \mathbf{D}_1$, so that Eq. (13) can be rewritten as

$$\delta \mathbf{f}_{z,2nd}^{p=1} = -\delta p_4 \mathbf{S}_4 + \delta p_1 \mathbf{S}_1. \quad (14)$$

This is the usual median mesh force differencing that works automatically for triangular subzonal pressures, and which has been used previously [6, 10]. This is illustrated by the force lobes drawn in Fig. 4b. The difference between the two corner force forms given by Eq. (12) and Eq. (14) is that more averaging of forces is present with Eq. (12), and less of an effect will be seen for the same values of subzone perturbed pressures. Although numerical results show that this problem is not very acute for subtriangular forces, it becomes much more severe for subquadrilateral forces. This is our next topic.

In Fig. 5a we show the same quadrilateral zone, along with half-edge vectors \mathbf{a}_i and median mesh normal vectors \mathbf{S}_i , that together define the subzonal quadrilaterals. These subzones as well as their associated dynamical grid points are labeled as numbers $1 \cdots 4$, while the center point and the edge midpoints labeled $5 \cdots 9$ comprise the nondynamical points. Proceeding as before we show in Fig. 5b the force contours associated with points $1 \cdots 9$ as though they were all dynamical. Denoting these forces by the vectors \mathbf{H}_i we have for those necessary to construct the corner force at point $p = 1$ the expressions

$$\begin{aligned} \mathbf{H}_1 &= \delta p_1 (\mathbf{a}_1 + \mathbf{a}_8) / 2 \\ \mathbf{H}_6 &= \frac{1}{2} [\delta p_1 \mathbf{a}_8 + \delta p_4 \mathbf{a}_7 + (\delta p_1 - \delta p_4) \mathbf{S}_4], \\ \mathbf{H}_7 &= \frac{1}{2} [\delta p_1 \mathbf{a}_1 + \delta p_2 \mathbf{a}_2 + (\delta p_2 - \delta p_1) \mathbf{S}_1], \\ \mathbf{H}_5 &= \frac{1}{2} [(\delta p_1 - \delta p_4) \mathbf{S}_4 + (\delta p_2 - \delta p_1) \mathbf{S}_1 + (\delta p_3 - \delta p_2) \mathbf{S}_2 + (\delta p_4 - \delta p_3) \mathbf{S}_3]. \end{aligned} \quad (15)$$

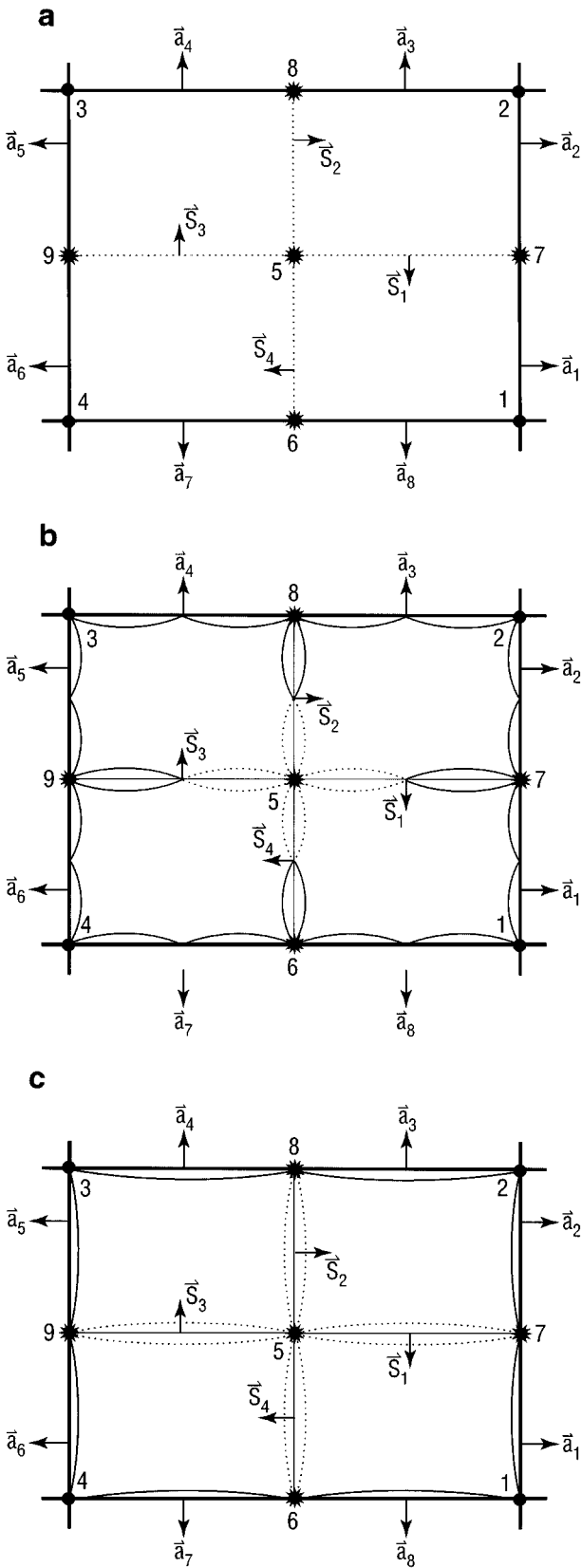
If we now distribute each of the forces \mathbf{H}_i associated with the nondynamical points $5 \cdots 9$ in proportion to the weights with which these points are enslaved to the dynamical points, then our first form for the perturbed corner force at point $p = 1$ becomes

$$\delta \mathbf{f}_{z,1st}^{p=1} = \mathbf{H}_1 + \frac{1}{2} (\mathbf{H}_6 + \mathbf{H}_7) + \frac{1}{4} \mathbf{H}_5. \quad (16)$$

Once again this differencing is not unique.

Aside from being systematic, the type of differencing of nondynamical points as given by Eq. (12) or Eq. (16) has some additional mathematical basis [11]. It arises from a variational principle that results in the gradient and divergence operators being negative adjoints of each

FIG. 5. (a) Quadrilateral zone: topology for subzonal quadrilateral volumes with nondynamical points $5 \cdots 9$. (b) Quadrilateral zone: force contours for quadrilateral subzonal forces differenced as Eqs. (15), (16). (c) Quadrilateral zone: force contours for quadrilateral subzonal forces differenced as Eqs. (17)–(20).



other. This in turn can be viewed as choosing the divergence as the “determining operator” from which to construct the gradient [14, 15]. This topic is discussed elsewhere in detail [13]. Here we wish to note what happens if we continue to subdivide our subzone quadrilaterals, all with separate Lagrangian masses and nondynamical defining points that are given as simple averages of adjacent points [11]. It is easy to see from the above that what we get is further averaging of the perturbed pressure forces, and that in general as we construct finer and finer subzones the effect of these forces is further decreased except for special smooth, one-dimensional motions of the dynamical points where they are not needed to counteract spurious vorticity anyway.

A force differencing that is preferable to the one just given can be constructed as follows: Eliminate the force contribution of the zone center \mathbf{H}_5 by combining its force lobes with those of the adjacent nondynamical midpoint members, just as was done in the triangular case. In addition, combine the edge vector \mathbf{a}_i contributions that are associated with the midpoints of the sides in favor of the dynamical grid points. This gives the force contours shown in Fig. 5c from which we define the new force vectors \mathbf{H}'_i . For points 1, 6, 7 these are given by

$$\begin{aligned}\mathbf{H}'_1 &= \delta p_1(\mathbf{a}_1 + \mathbf{a}_8), \\ \mathbf{H}'_6 &= (\delta p_1 - \delta p_4)\mathbf{S}_4, \\ \mathbf{H}'_7 &= (\delta p_2 - \delta p_1)\mathbf{S}_1,\end{aligned}\tag{17}$$

and analogously for the other points in Fig. 5c, except that now $\mathbf{H}'_5 = 0$.

The force contours shown in Fig. 5c lend themselves to a simple interpretation; namely, there are the subzonal forces $\mathbf{H}'_1 \cdots \mathbf{H}'_4$ that are computed along the coordinate-line mesh and directly applied to their respective dynamical points, and there are the “recoil” of these forces that are shown with respect to the median mesh as the force lobes $\mathbf{H}'_6 \cdots \mathbf{H}'_7$ associated with the side midpoints and the common center point of a zone. These two sets of forces, individually summed, are equal in magnitude and opposite in direction. Many discretizations of the subzonal forces can now be thought of as just different ways of redistributing the recoil forces to the dynamical points with the forces along the coordinate-line mesh fixed as stated. Our preferred way of doing this results in our second form of the subzonal forces in which one-half of each recoil force lobe $\mathbf{H}'_6 \cdots \mathbf{H}'_7$ is allotted to each of its adjacent dynamical points. Then the perturbed corner force at point $p = 1$ becomes

$$\begin{aligned}\delta \mathbf{f}_{z,2nd}^{p=1} &= \mathbf{H}'_1 + \frac{1}{2}(\mathbf{H}'_6 + \mathbf{H}'_7), \\ &= \delta p_1(\mathbf{a}_1 + \mathbf{a}_8) + \frac{1}{2}[(\delta p_1 - \delta p_4)\mathbf{S}_4 + (\delta p_2 - \delta p_1)\mathbf{S}_1],\end{aligned}\tag{18}$$

$$= \delta p_1(\mathbf{a}_1 + \mathbf{a}_8)/2 - \delta p_4\mathbf{S}_4/2 + \delta p_2\mathbf{S}_1/2,\tag{19}$$

$$= (\delta p_1 + \delta p_2)\mathbf{S}_1/2 - (\delta p_1 + \delta p_4)\mathbf{S}_4/2.\tag{20}$$

This equation has been written in several equivalent forms, all of which are important. From the forms given as Eqs. (18), (19) and the fact that $\mathbf{S}_1 - \mathbf{S}_4 = \mathbf{a}_1 + \mathbf{a}_8$ (cf., Fig. 5a) it can be seen that the direct force given by the first term of Eq. (19) is decreased over that in Eq. (18) by a factor of one-half because the recoil force given by $-\delta p_1(\mathbf{S}_1 - \mathbf{S}_4)/2$ just cancels this amount. Thus, this force differencing has a “merit factor” of one-half relative

to the triangular force differencing given by Eq. (14) where no recoil forces from a given point act back upon it.

A force differencing with a merit factor of unity for subzonal quadrilaterals can easily be constructed by specifying the corner force at point $p = 1$ to be

$$\delta \mathbf{f}_{z,3rd}^{p=1} = \delta p_1 (\mathbf{a}_1 + \mathbf{a}_8) - \delta p_2 \mathbf{a}_3 - \delta p_4 \mathbf{a}_6. \quad (21)$$

In this instance the recoil force from a given point is also taken up entirely by differing adjacent points. In the above form the corner force on point 1 includes a recoil force from the opposite half-edge vectors \mathbf{a}_3 and \mathbf{a}_6 . We prefer not to use this form because for distorted grids it is not very symmetric, whereas for Eq. (19) we have the previously noted expression $\mathbf{S}_1 - \mathbf{S}_4 = \mathbf{a}_1 + \mathbf{a}_8$, which allows us to reduce it to the form given as Eq. (20). This equation says that the total perturbed corner force is simply the average of the adjacent perturbed pressures applied to the median mesh, which is intuitively appealing and symmetric.

We actually code the form given as Eq. (18) after multiplying it by a factor of two. Then in all quoted results the merit factor when referenced to this form is unity. There is an important reason for doing this. For the case where we wish to preserve cylindrical symmetry in Cartesian geometry, or spherical symmetry in cylindrical geometry for a wide range of conditions this is the only form that will, with grid modifications, yield this desired result. This is explained elsewhere [17] where a modification of both grid vectors \mathbf{a}_i and \mathbf{S}_i must be performed to achieve this goal when subzonal pressure forces are present. However, in the case where such symmetry is present only two different values of perturbed subzonal pressures, as opposed to the usual four, occur and one of the last two terms of Eq. (18) will always vanish. After this grid modification Eq. (18) is no longer equal to either Eq. (19) or Eq. (20). For triangular subzone pressures there is no subzonal force differencing that will preserve the above noted symmetries for a wide range of conditions.

5.1. Automation of Merit Factor

Although one can specify different values of the merit factor on input for a given run, this factor can be easily automated based on the variation of the values of the subzonal densities relative to the mean density of a zone. We define the zone variable x as the maximum subzone density in a given zone minus the mean density divided by the mean density, $x \equiv \sup(\delta\rho)_z / \rho_z$. Then based on this variable the merit factor for a zone z , denoted by M_f , is specified by

$$M_f = \left[.5\alpha_1 \left(1 - \cos\left(\frac{\pi x}{2\alpha_2} \right) \right) \right]^n, \quad (22)$$

for $x \leq 2\alpha_2$, and as

$$M_f = \alpha_1^n, \quad (23)$$

for $x > 2\alpha_2$. In the above expressions we have found the settings $\alpha_1 = \sqrt{2}$, $\alpha_2 = 0.1$, and $n = 2$ to be approximately optimum for a wide range of problems. These expressions give a value for the merit factor that varies monotonically and with a continuous first derivative with respect to the variable x between the range of values 0.0 to α_1^n with a point of inflection at $x = \alpha_2$.

Heuristically, we find that if $\delta\rho/\rho_z \geq 0.1$ then the merit factor should be increased, while if $\delta\rho/\rho_z \leq 0.1$ then it should be decreased, relative to the interpolation obtained using a linear slope between 0.0 and α_1^n in order to achieve near optimum results on test problems. The latter is very much the case for low-speed flow calculations. For example, we have performed simulations of Rayleigh–Taylor instability with subzonal forces and we observe that in order to obtain the correct linear growth rate the merit factor must be less than about 0.25. Then we can run far into the nonlinear regime without grid tangling. The results appear qualitatively correct; detailed comparisons to Eulerian code results will be a topic of future work. For high speed flow calculations, such as some given in Section 7, a value of the merit factor greater than one is required to achieve results close to the optimum that can be obtained for fixed values of this factor. With the values quoted for α_1 , α_2 , and n all of these problems can be run with near optimum results.

Another simple but effective strategy for setting M_f is to perform a sequence of runs using coarse spatial resolution to determine the smallest constant value of M_f that is consistent with grid integrity. Then the spatial resolution can be increased to give the desired accuracy. We do not find the value of M_f to be very sensitive to grid resolution.

6. SUBTRIANGLES VERSUS SUBQUADRILATERALS

As we have discussed earlier, the use of quadrilateral subzones associated with corner masses as auxiliary Lagrangian elements is a natural choice. However, it is useful to review the difficulties and limitations of using triangles as subzone grid elements since this has been the choice historically, mostly because difference schemes with subtriangles are conceptually simpler to formulate. This is because, as seen, the force differencing can simply be taken along the median mesh.

A limitation of triangles as grid elements is the stiffness problem for compressible flow. There are also problems associated with the use of triangles as grid elements for incompressible flow. The latter are discussed at length in the paper by Fritts and Boris [18] where this goes under the keywords “counting problem” or “grid locking problem.” For compressible flow, grid “stiffness,” an artificial resistance to the true fluid motion, can be best seen by contrasting a planar flow situation to that of a convergent flow. This is shown in Figs. 6a, 6b where in Fig. 6a we show a planar flow interacting with a rigid wall; in Fig. 6b we show a flow that stagnates with respect to a center of convergence. A quadrilateral grid with an underlying triangular subzoning is shown. The question to be asked here with regard to stiffness is: Does the collapse of two geometric grid points into a common point imply a true singularity in the flow field? In the planar case shown in Fig. 6a the answer to this question is affirmative, since the flow tries to collapse all four triangles of the quadrilateral and a pressure necessary to resist this occurrence is the correct physical effect. However, in Fig. 6b, where a convergent flow is shown, the physical effect is for the quadrilateral to become degenerate, forming a triangle, and no physical flow singularity occurs. A triangular zoning yields the artificially stiff triangles shown as shaded regions, which in the limit of convergence lose their interior edge resulting in zero volume, and give rise to a totally unphysical grid singularity. This leads to unphysically high pressures and consequent resistance to fluid flow [19].

It is for the above reason that we choose quadrilaterals over triangles as zone elements. For subzonal grid elements, as seen, this difficulty does not diminish. In addition, subzone quadrilaterals nicely match the quadrilateral zone structure. Thus, for a propagating front of constant phase it is possible to achieve grid alignment, wherein the coordinate lines lie nearly

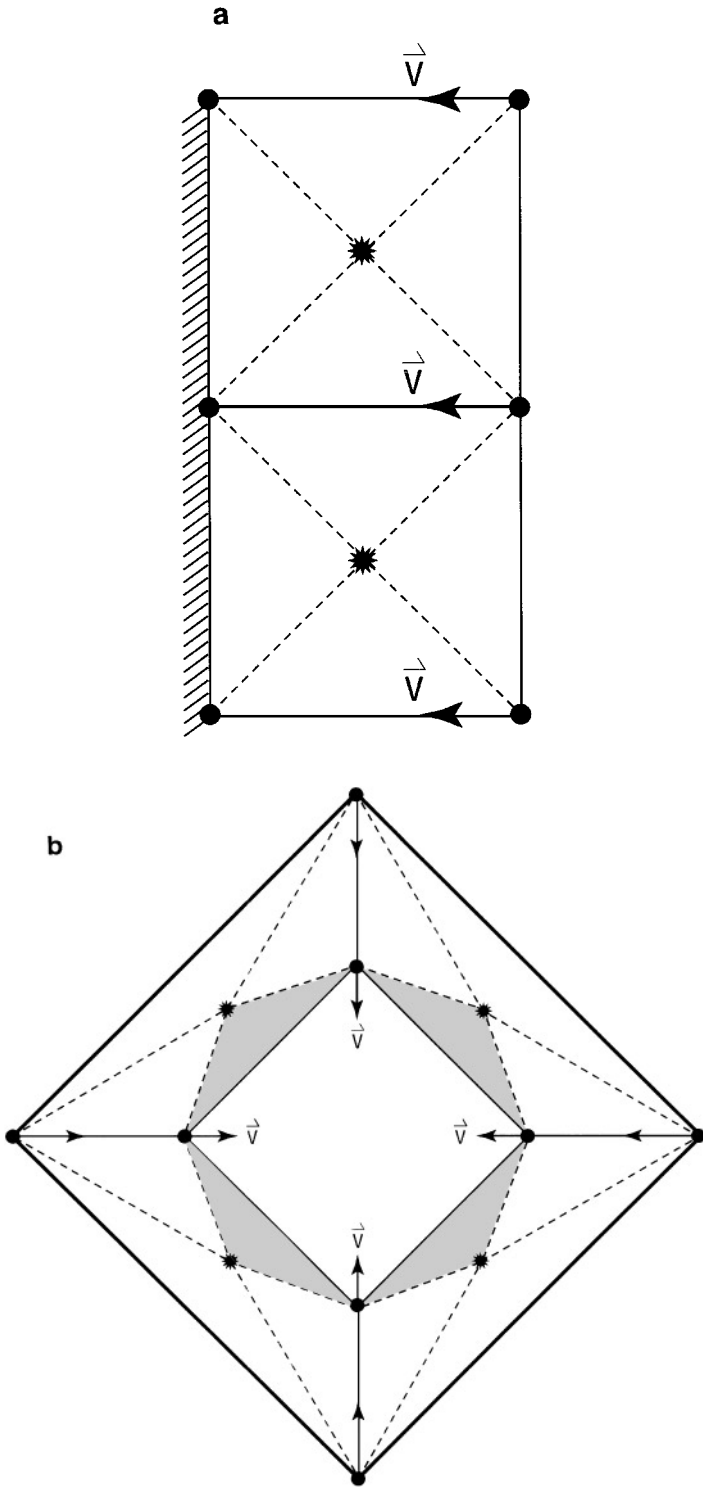


FIG. 6. (a) Quadrilateral zones with triangular subgrid-planar flow. (b) Quadrilateral zones with triangular subgrid-convergent flow.

along and perpendicular to the phase front. Finally, studies by Goloviznin *et al.* [11] utilizing a different approach come to very similar conclusions. In this work results of a normal mode analysis of the linearized difference equations associated with a quadrilateral grid with subtriangular and subquadrilateral zones are given. The smaller the natural frequency ω of a grid vertex the more movement it is allowed, and the less “rigid” is the numerical differencing. They find that if one measures the natural frequency ω of a purely quadrilateral grid as unity, then for such a grid with subtriangles $\omega = \sqrt{1.5}$, and for subquadrilaterals $\omega = \sqrt{1.25}$. If one triangulates a quadrilateral grid poorly, with diagonals all drawn in one sense of direction, a much higher value $\omega = \sqrt{5}$ is obtained indicating a much stiffer grid.

In three dimensions the competition between tetrahedra and hexahedra can be viewed in much the same manner as above because we would like our three-dimensional results to reduce to two-dimensional ones in the limit of an ignorable coordinate. Since tetrahedra reduce to triangles in two dimensions, this requirement argues for the use of grid elements more general than tetrahedra.

7. NUMERICAL RESULTS AND DISCUSSION

Numerical results are presented to show both the effectiveness of our procedure and also the sensitivity of the calculations to the merit factor that affects the strength of the subzonal forces. All results are run with subzonal quadrilateral forces using the differencing given by Eq. (18). We use an ideal gas equation of state for all problems except the bending beam case. An edge-centered artificial viscosity is employed to capture shocks [9]. The underlying differencing of the hydrodynamics equations is a control volume scheme, except for the Lazarus implosion problem where we use the area-weight variant [13, 17] in cylindrical geometry. All changes in internal energy are calculated compatibly so that total energy is always conserved to roundoff error [13]. For the sake of brevity we sometimes give only partial problem setups and reference where the complete specifications can be found; all of these have been previously published elsewhere.

Our first test example is the bending beam problem of Flanagan and Belytschko [4] in two-dimensional Cartesian ($x - y$) geometry. This problem readily develops a virulent hourglass distortion. It consists of a perfectly elastic beam that we take to be 100 cm in length and 50 cm in width that is perfectly hinged at the vertical midpoint locations of both of its ends (25 cm from its base); the force of gravity acts downward (negative y direction). This region is discretized with 16×32 zones. The beam obeys a stiffened gas equation of state [20] where the pressure p and sound speed c_s are given in terms of the density ρ and the specific internal energy e by

$$p = a^2(\rho - \rho_0) + (\gamma - 1)\rho e, \quad (24)$$

$$c_s^2 = a^2[\gamma - (\gamma - 1)\rho_0/\rho] + \gamma(\gamma - 1)e. \quad (25)$$

For this problem we set $\rho_0 = 8.0 \text{ gm/cm}^3$, $a^2 = 1. \times 10^{11} \text{ cm}^2/\text{s}^2$, and $\gamma = 3$. The downward force of gravity is $g = 1. \times 10^8 \text{ cm/s}^2$. The initial density is ρ_0 ; initial velocity, specific internal energy, and stress deviators are all zero. All boundaries are free except for the two hinged points for which $\mathbf{v}(t) = 0$. The stress deviators associated with material strength are updated in the usual manner by integrating their time derivatives; these are equal to the elastic shear modulus G times the traceless symmetric strain rate tensor that is computed in the zone centers. The stress deviators are thus zone centered, and are never subzonal in

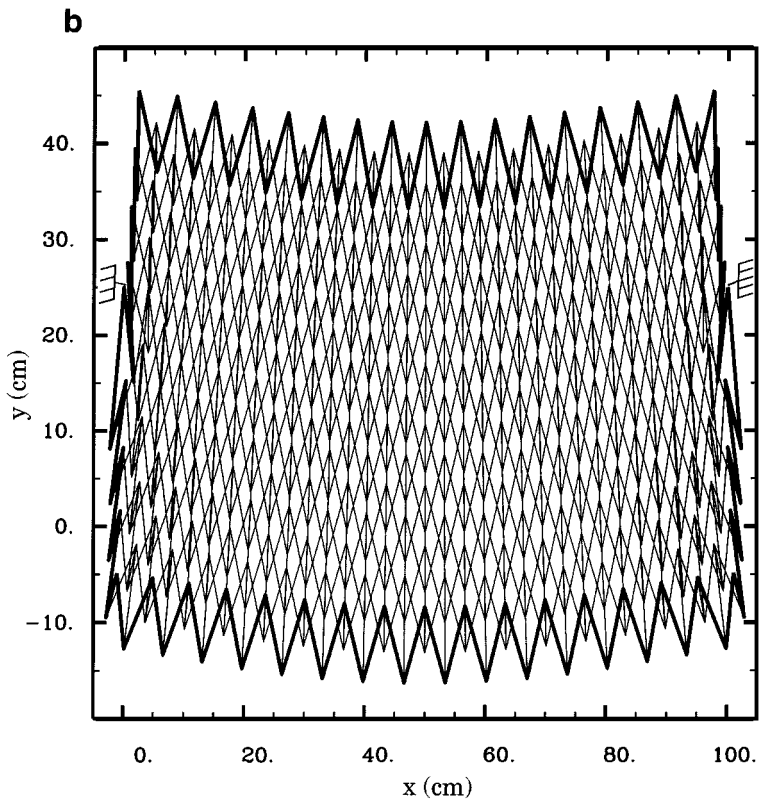
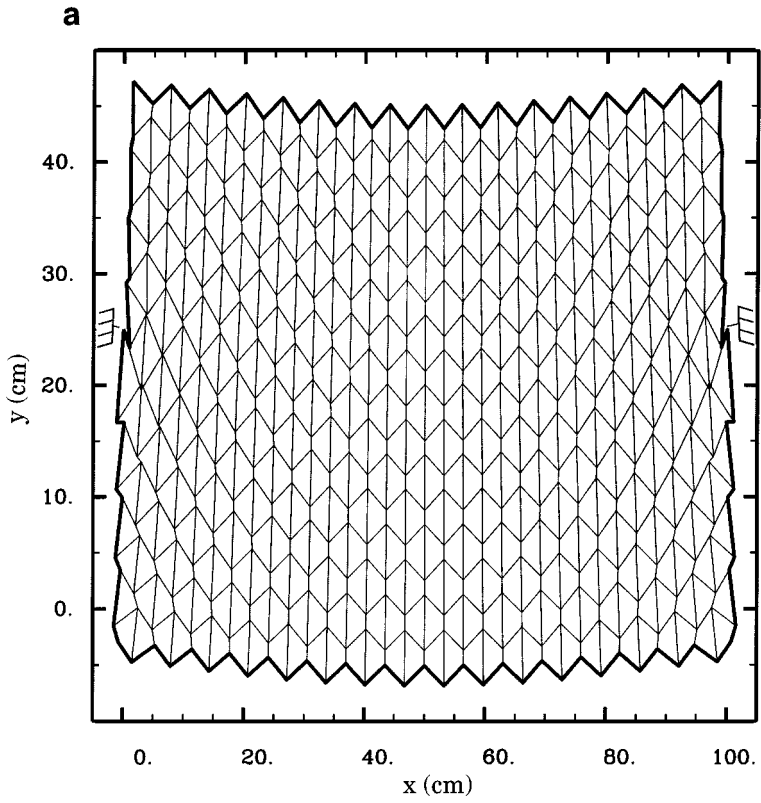
the sense of the pressures used in this paper. Material strength forces are computed as the divergence of the stress deviators using the usual control volume differencing implemented relative to the median mesh. For this case we set $G = 1. \times 10^{12}$ dynes/cm².

The beam is not initially in force equilibrium and begins to execute an elastic oscillation. In the first simulation of this problem, shown in the four parts of Fig. 7, we use no subzonal pressure forces and no artificial viscosity. The beam is shown at the time $t = 3.5 \times 10^{-4}$ s in Fig. 7a where a pure hourglass distortion of the entire grid has developed but the zones have not yet become overlapping. (The supports are indicated by the hatched symbol at the middle of both ends.) In Fig. 7b the beam is shown at time $t = 5.5 \times 10^{-4}$ s where zone overlapping, although severe, still allows distinct zones to be visualized. However, this problem can be run indefinitely without numerical failure and is continued until the time $t = 0.01$ s. By this time the grid completely separates and appears as a black smear that extends to -5000 cm in the negative vertical y direction. In Figs. 7c, 7d are shown the velocity in the vertical direction as a function of time of two adjacent points numbered (17, 17) and (17, 18) that initially lie at the top center of the horizontal boundary of the beam. Notice that the first point (17, 17), as seen from Fig. (7c), undergoes just over seven periods of sinusoidal motion about zero velocity; whereas the adjacent point (17, 18), whose velocity versus time is shown in Fig. 7d, displays a linear increase in velocity in the negative y direction with a slope of 10^8 cm/s², which just matches the value of gravity employed in the simulation. This pattern is repeated by every other point across the entire grid except for the two hinged boundary points. What is seen is a perfect hourglass pattern that results from near perfect cancellation of all forces except that of gravity at every other point. Thus, half of the points free-fall under a constant gravitational field while the other half execute sinusoidal motion that is approximately that of the correct oscillating beam solution with material stress forces calculated from highly elongated zones whose length increases as $gt^2/2$.

As just computed, this problem is ill-posed in that minor changes in the initial and boundary conditions (using an odd number of zones or hinging the two boundary points slightly asymmetrically) will break this decoupling pattern of every other point. In this instance a highly distorted and virtually random pattern of points results and the code will crash much before the final time shown. If this problem is run with all points at either end hinged with zero velocity then the hourglass pattern will still develop but will not be nearly as virulent as that shown with just fixing single points at either end. How hourglass motion will be constrained by altering the boundary conditions in any given situation is not a priori obvious.

In the first three parts of Fig. 8 results are given for this problem with subzonal pressure forces using a constant merit factor of 0.25 and with no artificial viscosity. The grid with velocity vectors at the points is shown in Fig. 8a at the time $t = 5.5 \times 10^{-4}$ s. No hourglass distortion is present at this time or at any other time throughout the run. In Fig. 8b is shown the same plot but at time $t = 8.5 \times 10^{-4}$ s when the grid velocity vectors have just changed sign from negative to positive (this could be at any such time of several in

FIG. 7. (a) Bending beam problem: grid at time $t = 3.5 \times 10^{-4}$ s, artificial viscosity and subzonal pressure forces off. (b) Bending beam problem: grid at time $t = 5.5 \times 10^{-4}$ s, artificial viscosity and subzonal pressure forces off. (c) Bending beam problem: vertical velocity versus time for point (17, 17). (d) Bending beam problem: vertical velocity versus time for point (17, 18).



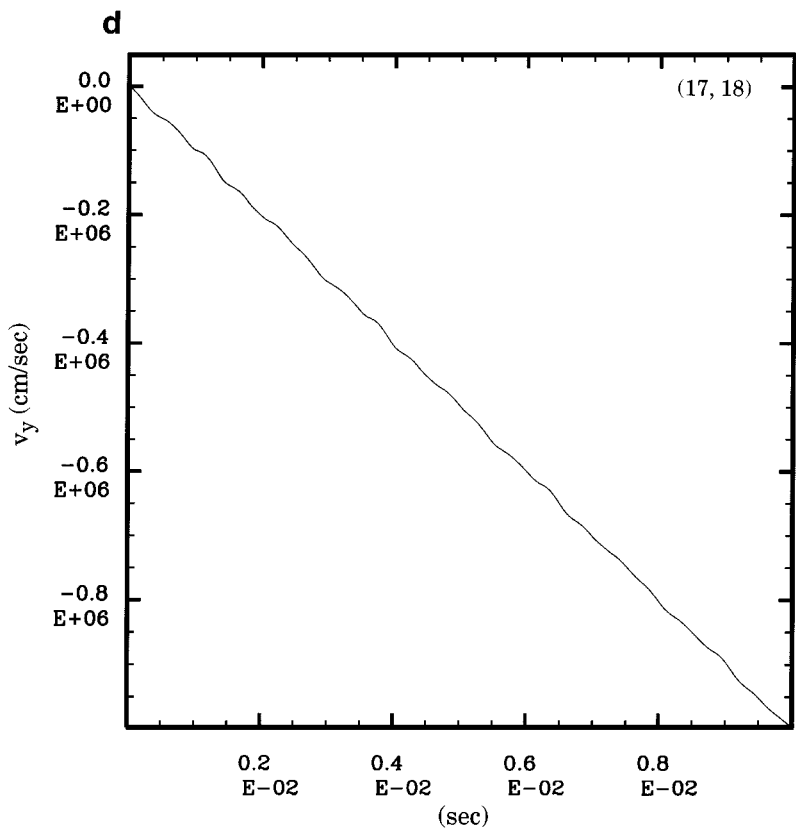
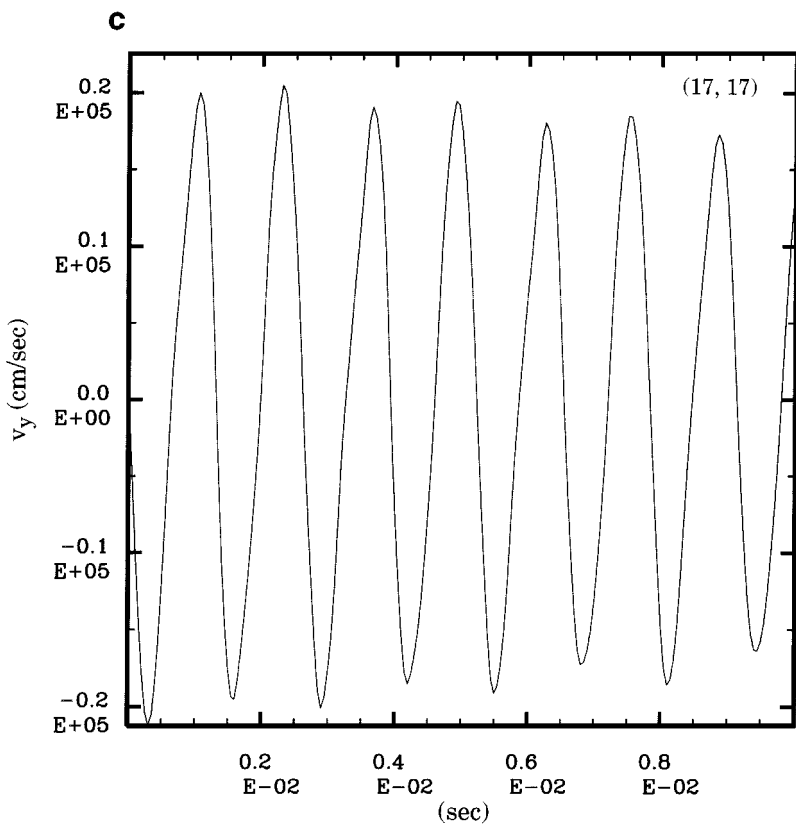


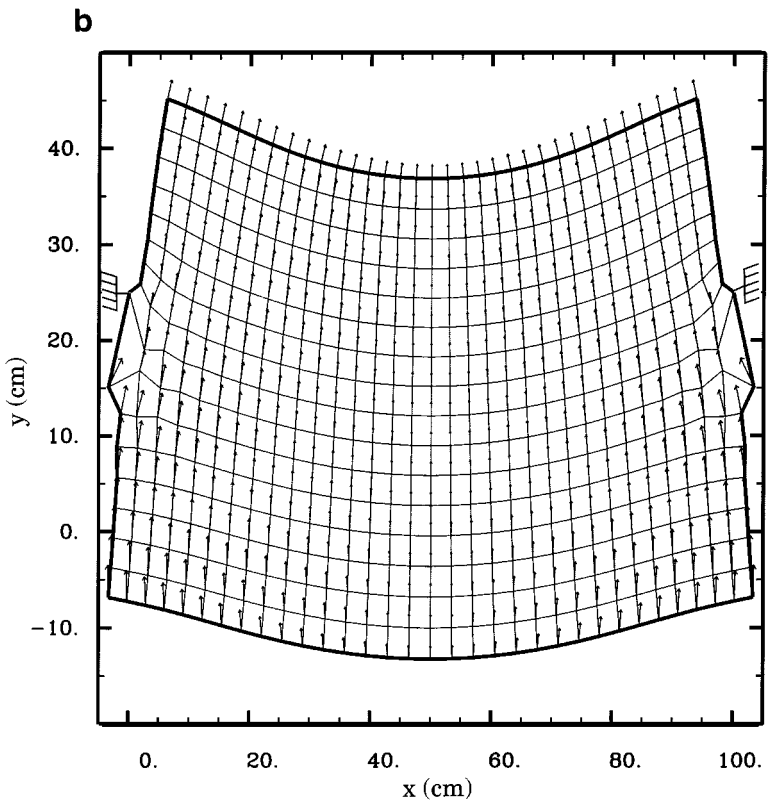
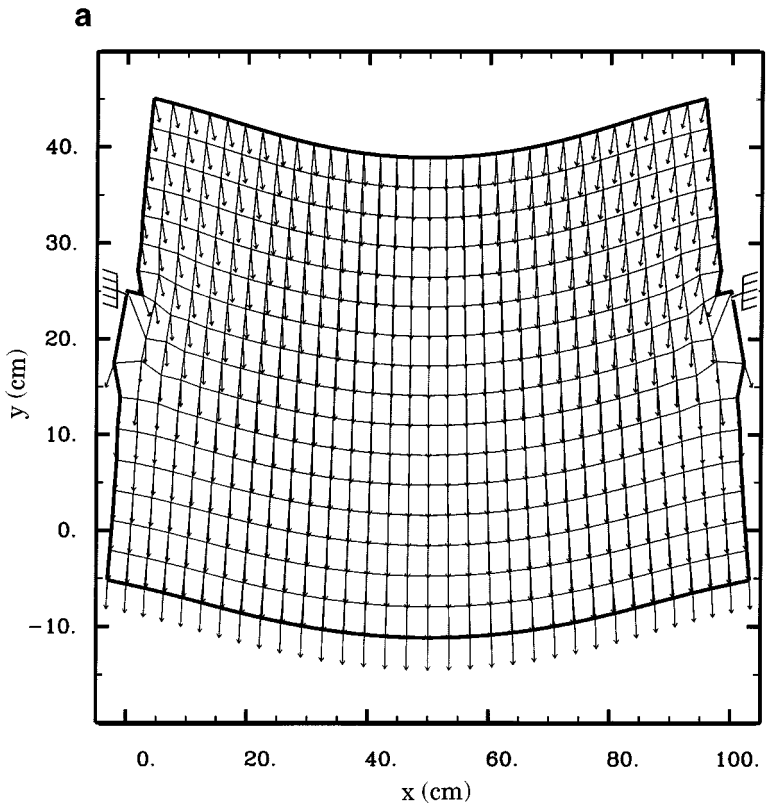
FIG. 7—Continued

this run) corresponding to the maximum amount of bending of the beam in any oscillation period. One-half of a cycle later the beam returns to its initial position and the velocity vectors change sign from positive to negative as shown in Fig. 8c. The velocity of the point (17, 17) in the vertical direction with respect to time is shown in Fig. 8d as the curve that has the highest magnitude of oscillation, and is seen to be approximately undamped. All other points of this simulation, except for the two hinged boundary points, exhibit this same oscillatory behavior with magnitudes that vary somewhat depending on their initial location. Note that this curve is qualitatively similar to that shown in the extreme hourglass case of Fig. 7c: the latter has a somewhat higher oscillation frequency and a smaller amplitude. The sensitivity of these results to the number of zones used and placing of the boundary points, that was present in the previous case, has been completely removed by the use of subzonal forces. The curves with smaller oscillation amplitude in Fig. 8d are a part of the next topic.

This problem is next run with the merit factor set to zero so that subzonal pressure forces are turned off but with the aforementioned edge-centered artificial viscosity turned on with standard settings [9]. The grid with velocity vectors is shown in Fig. 9a at time $t = 5.5 \times 10^{-4}$ s. It is seen that a very substantial resistance to the development of the hourglass pattern has been achieved at this time. This pattern shows itself only near the two supports. However, the velocity field is seen to be damped, over that at the same time in Fig. 8a where no viscosity is present, both in magnitude and with respect to the direction of these vectors; they are much more grid aligned than in Fig. 8a. The grid with velocity vectors is shown again in Fig. 9b at the latter time of $t = 9. \times 10^{-4}$ s just after this calculation terminates due to excessive grid distortion near the supports. At this time the beam is about to reverse direction of oscillation as can be seen from the velocity vectors, but the hourglass pattern has reasserted itself. Thus, what is seen is that while an edge-centered artificial viscosity can provide some resistance to hourglass motion it is not nearly as effective as the subzonal pressure force method, and comes at the price of excessive dissipation. To further clarify this latter point we return to Fig. 8d where the curve with the middle-size amplitude is the vertical velocity of point (17, 17) versus time for this problem run with both a merit factor of 0.25 for the subzonal pressure forces and with the artificial viscosity turned on using standard parameters. The subzonal pressure forces eliminate all hourglass motion without the need for artificial viscosity. While the period of oscillation does not change the amplitude is seen to decrease with time. The curve with the smallest magnitude in Fig. 8d shows the result for this same problem except that the limiters on the artificial viscosity have been turned off so that this viscosity acts more strongly resulting in an enhanced damping of the oscillation amplitude, as can be seen.

If this problem is run with a fixed merit factor of less than about 0.1 severe hourglass distortion begins to occur; if it is run with a fixed merit factor of 1.0 the amplitude of the

FIG. 8. (a) Bending beam problem: grid with velocity vectors at time $t = 5.5 \times 10^{-4}$ s, artificial viscosity off, subzonal pressure forces on, merit factor = 0.25. (b) Bending beam problem: grid with velocity vectors at time $t = 8.5 \times 10^{-4}$ s (maximum excursion), artificial viscosity off, subzonal pressure forces on, merit factor = 0.25. (c) Bending beam problem: grid with velocity vectors at a time of minimum excursion, artificial viscosity off, subzonal pressure forces on, merit factor = 0.25. (d) Bending beam problem: vertical velocity versus time for point (17, 17), subzonal pressure forces on, merit factor = 0.25. Three cases: maximum amplitude-artificial viscosity off, middle amplitude-artificial viscosity on and limiters on, minimum amplitude-artificial viscosity on and limiters off.



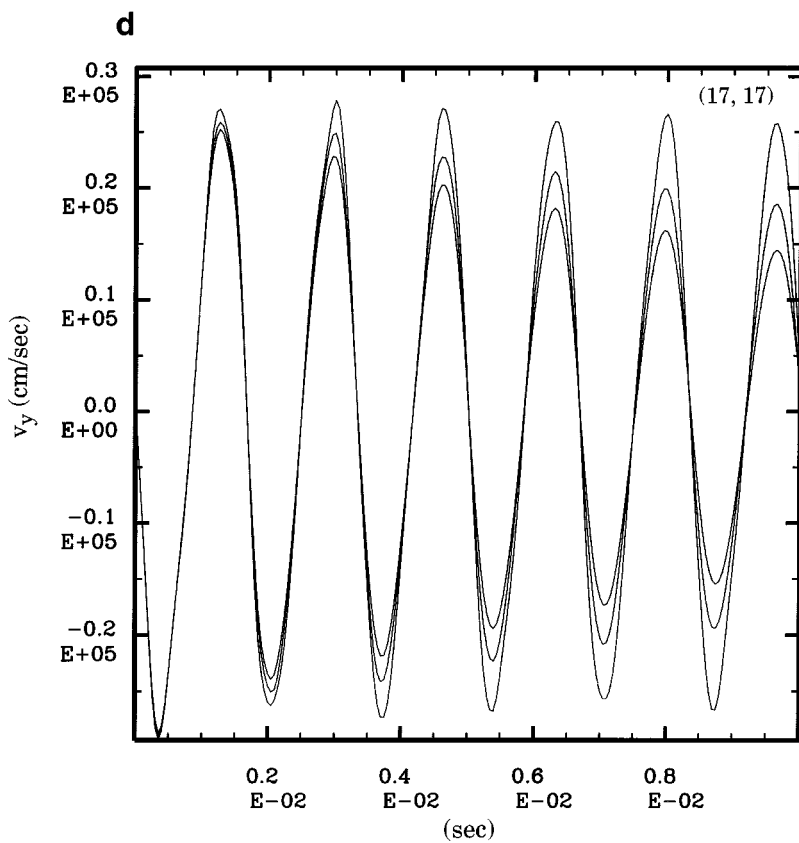
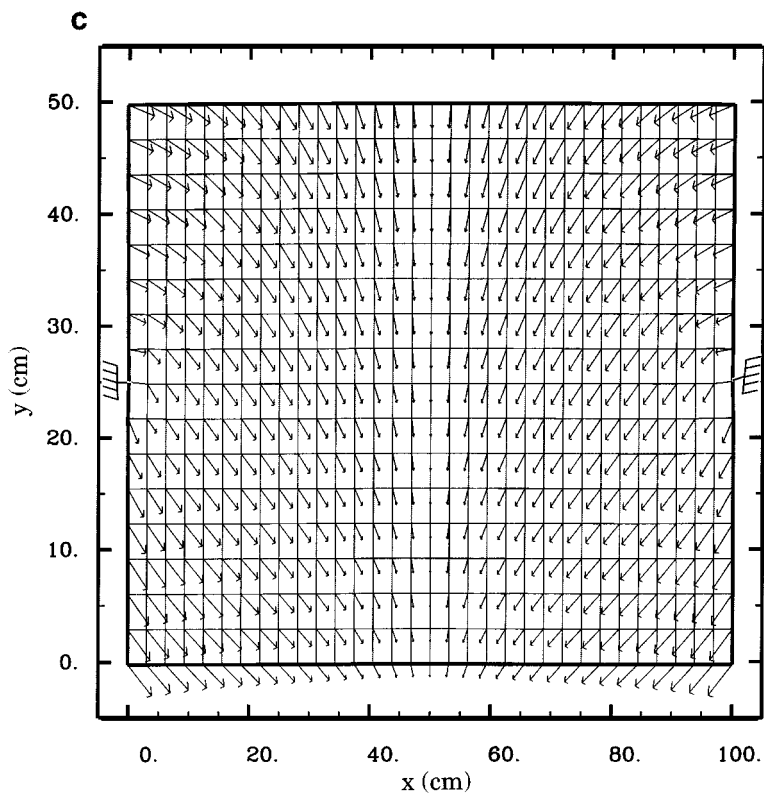


FIG. 8—Continued

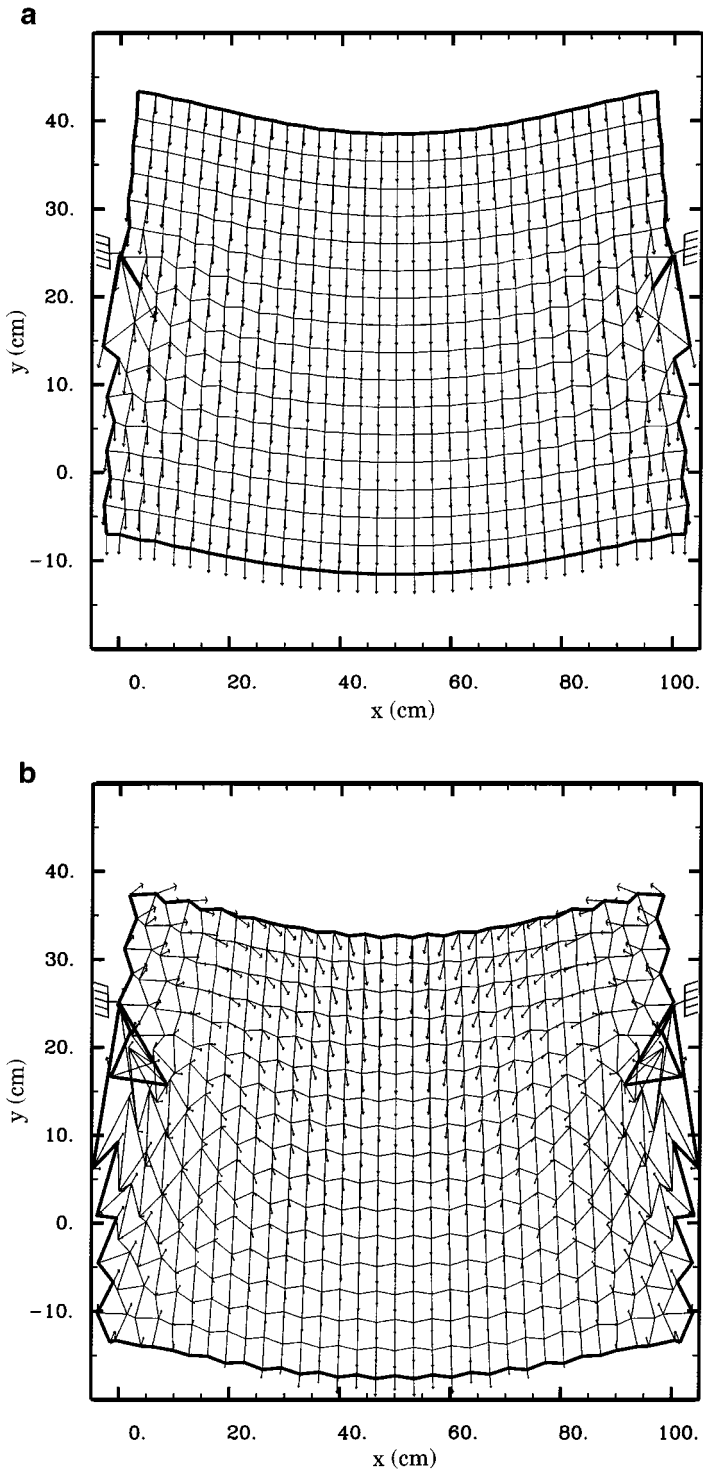


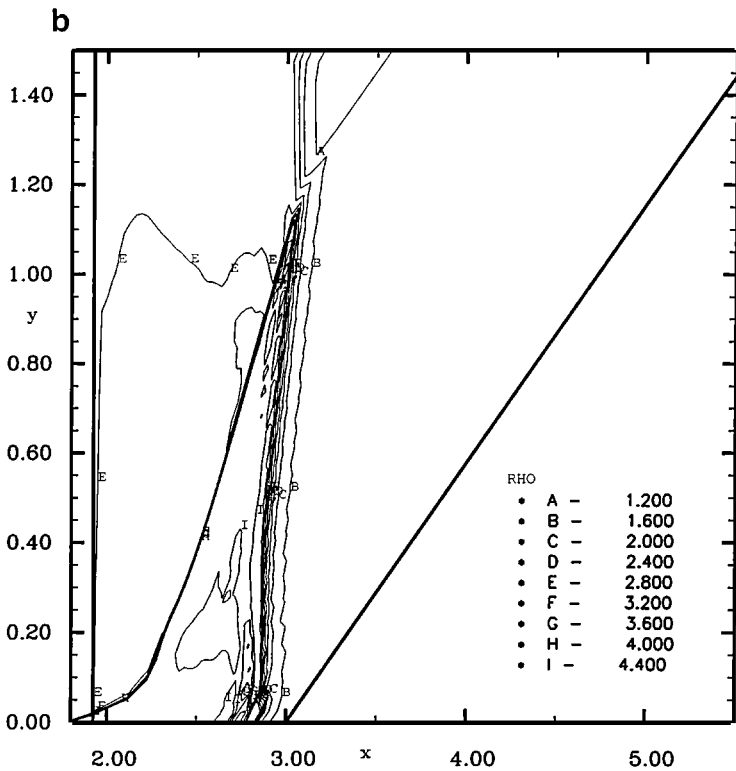
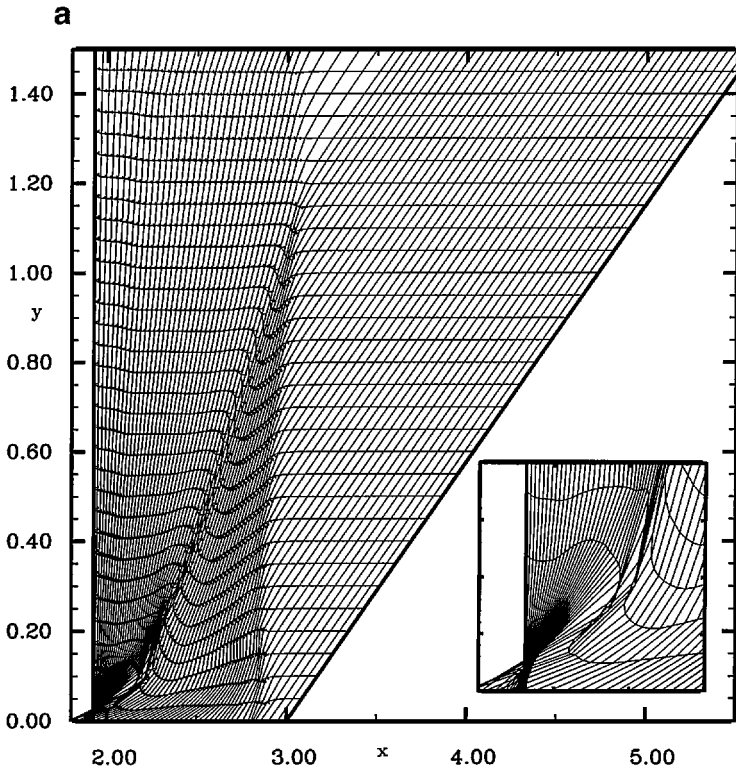
FIG. 9. (a) Bending beam problem: grid with velocity vectors at time $t = 5.5 \times 10^{-4}$ s, artificial viscosity on: subzonal pressure forces off. (b) Bending beam problem: grid with velocity vectors at time $t = 9.0 \times 10^{-4}$ s (run termination), artificial viscosity on: subzonal pressure forces off.

oscillations is nearly the same as that seen in Fig. 8d for otherwise identical run parameters; however, the frequency of the oscillations does increase by about 10%. The reason for this appears to be due to a somewhat larger effective sound speed.

We now consider a shock refraction problem in Cartesian geometry using the same grid setup as Dukowicz and Meltz [5]. In this problem a piston moves from the left sending a shock wave through an initially cold material of unit density with a grid that is tapered so that its right boundary is at an angle of 60° relative to the vertical. This shock then becomes incident on a second grid that is slanted but uniformly spaced at an angle of 60° . Reflective boundary conditions are applied to the top and bottom of both grids. The region composed of the second grid has an initial density of 1.5. The problem is run to a time $t = 1.3$ just before the shock starts to run off the second grid. We show results at this time. In Figs. 10a, 10b are shown the grid with velocity vectors and a contour plot of the density, respectively, using our base scheme and without any subzonal forces. We see that some grid tangling has occurred in the lower left hand corner next to the driving piston and lower reflective boundary. An enlarged portion of the grid in this region is displayed in the lower right hand corner of Fig. 10a. The density contour shows a sharp contact discontinuity at the initial boundary of the two regions. The importance of this problem is that we have both physical vorticity and spurious grid distortion present [5]. In Figs. 10c, 10d are shown the same results except that subzonal pressure forces have been utilized with a constant merit factor of 0.25. All grid tangling has disappeared; the density contours have only changed slightly from before. The same case has been run with a merit factor of 1.0. The grid at this time looks identical to that of Fig. 10c. In Fig. 10e we display the contour of density for this run and note that it has changed only slightly from the previous results. The region near the contact discontinuity, where physical vorticity is present, is virtually the same in all cases.

Next, we show results of the Saltzman piston problem [5, 21]. In this example a piston moves with unit velocity from the right sending a shock across a grid that is skewed with respect to the vertical with a one-half sinwave perturbation. The initial density is unity and internal energy is zero. The shock reflects off a fixed boundary at the left end. We run this problem in cylindrical ($r - z$) geometry with reflective boundary conditions at the z -axis and at the outer radial boundary of $r = 0.1$. The reflective boundary at the z -axis is through the center of the zone and there are no grid points at $r = 0$. Results for this problem are shown at time $t = 0.8$ when the shock has reflected from the left boundary and is moving back towards the driving piston. In Figs. 11a, 11b are shown the grid and a contour plot of the density, respectively, for our standard scheme with no subzonal pressure forces. All grid distortion is spurious since this is a purely one-dimensional problem. The correct answer for the density is 4.0 in the singly shocked region and 10.0 in the doubly shocked region. Significant deviations from this result can be seen. Again we show in Figs. 11c, 11d the grid and density contours at this time but using subzonal pressure forces with a merit factor of 1.0. Some very minor distortion remains but the answers are extremely close to the true solution.

FIG. 10. (a) Shock refraction problem: grid with velocity vectors at time $t = 1.3$ —zero merit factor. (b) Shock refraction problem: density contours at $t = 1.3$ —zero merit factor. (c) Shock refraction problem: grid with velocity vectors at time $t = 1.3$ —merit factor = 0.25. (d) Shock refraction problem: density contours at $t = 1.3$ —merit factor = 0.25. (e) Shock refraction problem: density contours at $t = 1.3$ —merit factor = 1.0.



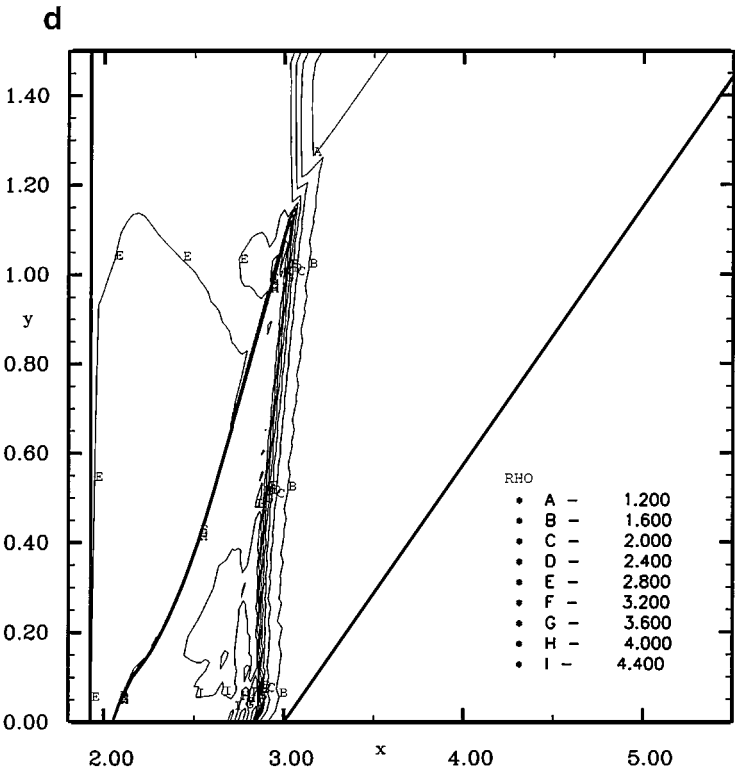
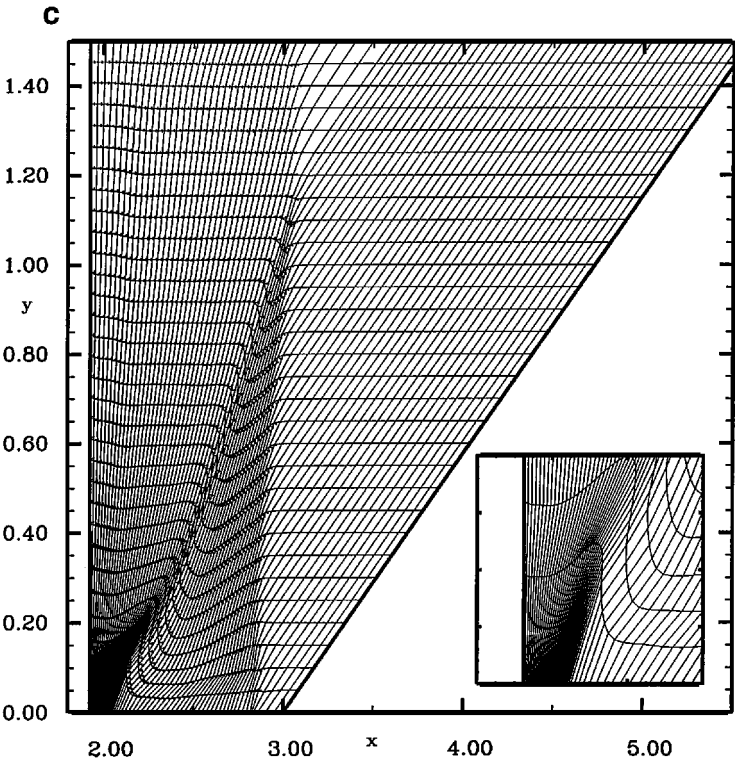


FIG. 10—Continued

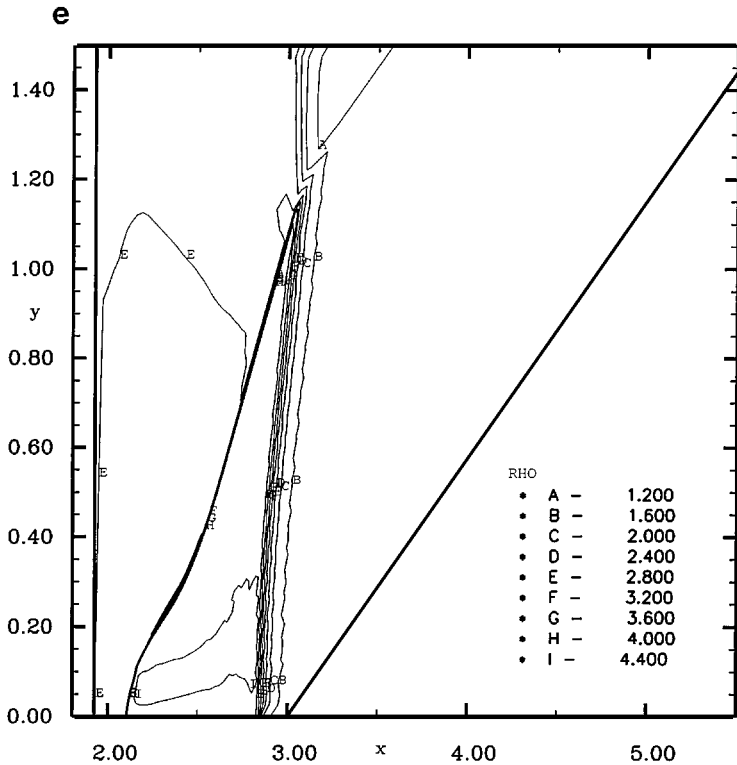
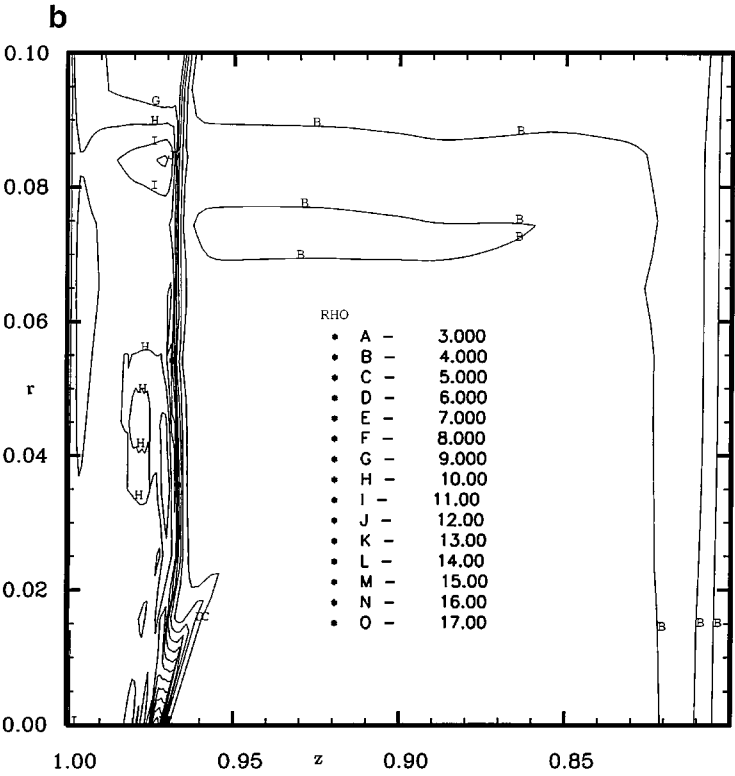
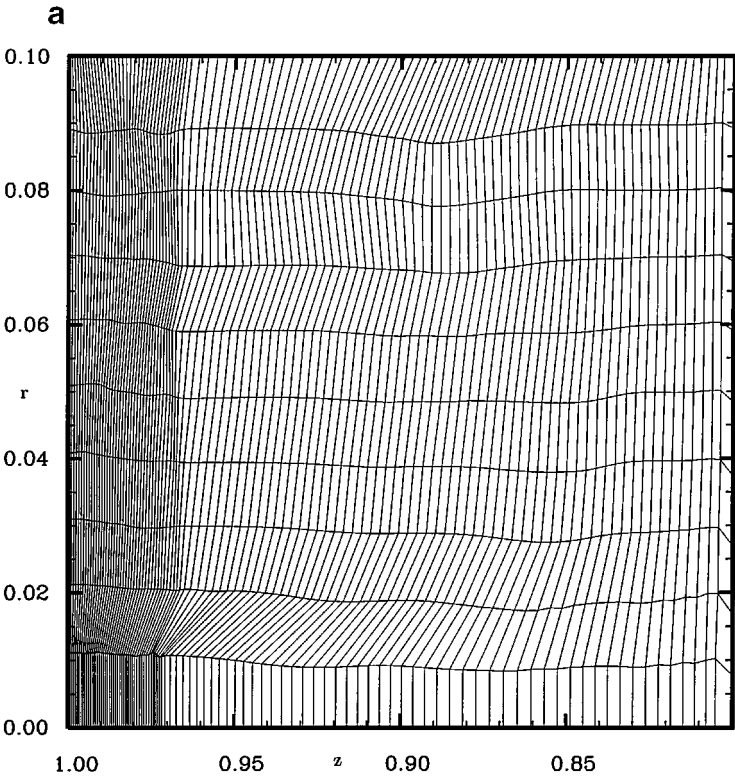


FIG. 10—Continued

In Fig. 12 we again show results using the Saltzman piston problem but this time for very high aspect ratio zones. Instead of the unit aspect ratio of the initial problem, we simply extend the radial, and ignorable, direction by a factor of 10^4 . This illustrates the long-thin zone problem mentioned at the beginning of this paper [6] as can be seen from the massive grid distortions shown in Fig. 12a. This figure shows the result from our standard algorithm at time $t = 0.8$ without subzonal forces. That the grid distortion for this case should be much worse than for the unit aspect ratio case is not a priori obvious since the size of the perturbation of the initial grid across the vertical length is constant. That is, the shock wave is more perpendicular to the vertical lines by a factor of 10^4 over the unit aspect ratio case. This places the directional perturbation of the grid relative to the solution at truncation error levels. In Fig. 12b is shown the grid for the same case but using subzonal forces with a merit factor of 1.0. While this result is much improved and no grid tangling is present, the grid still departs from a planar front where the reflected shock is moving back towards the piston. The results shown in Fig. 12c has subzonal forces with a merit factor equal to 2.0. This is nearly perfect with densities extremely close to the true values and a coherent shock front. It is easy to construct highly curved but non-overlapping initial grids at high aspect

FIG. 11. (a) Saltzman piston problem: grid at time $t = 0.8$, unit aspect ratio, merit factor = 0.0. (b) Saltzman piston problem: density contours at time $t = 0.8$, unit aspect ratio, merit factor = 0.0. (c) Saltzman piston problem: grid at time $t = 0.8$, unit aspect ratio, merit factor = 1.0. (d) Saltzman piston problem: density contours at time $t = 0.8$, unit aspect ratio, merit factor = 1.0.



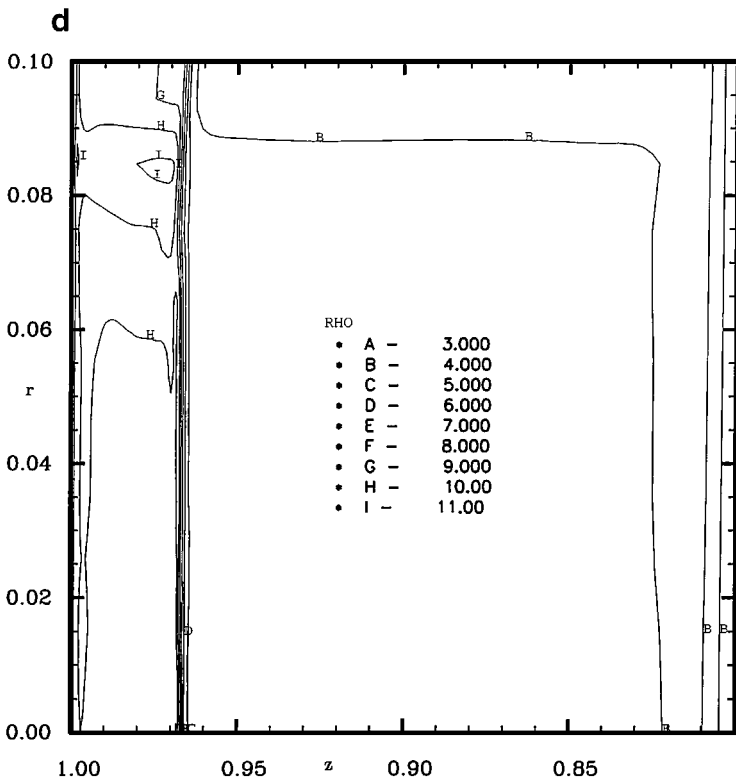
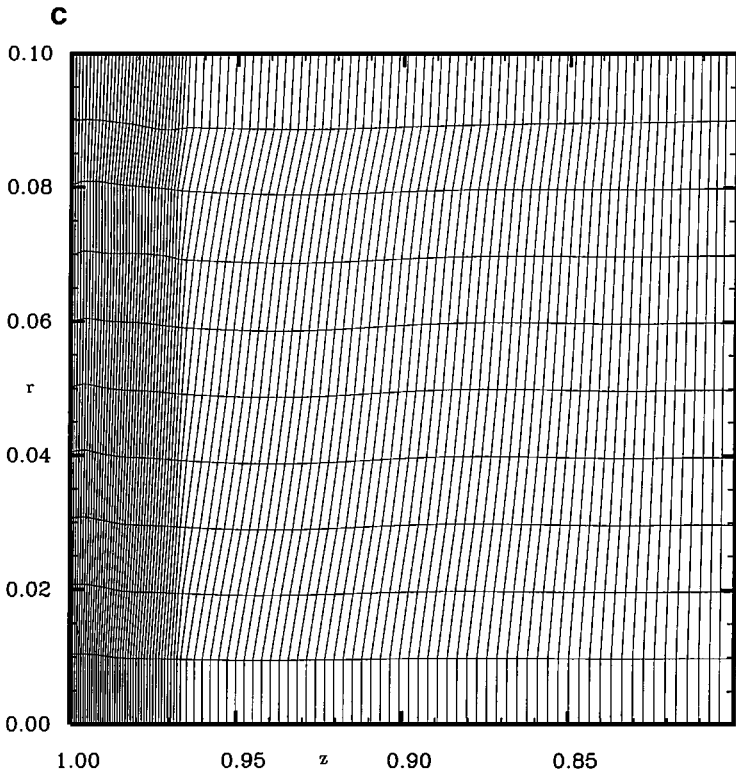


FIG. 11—Continued

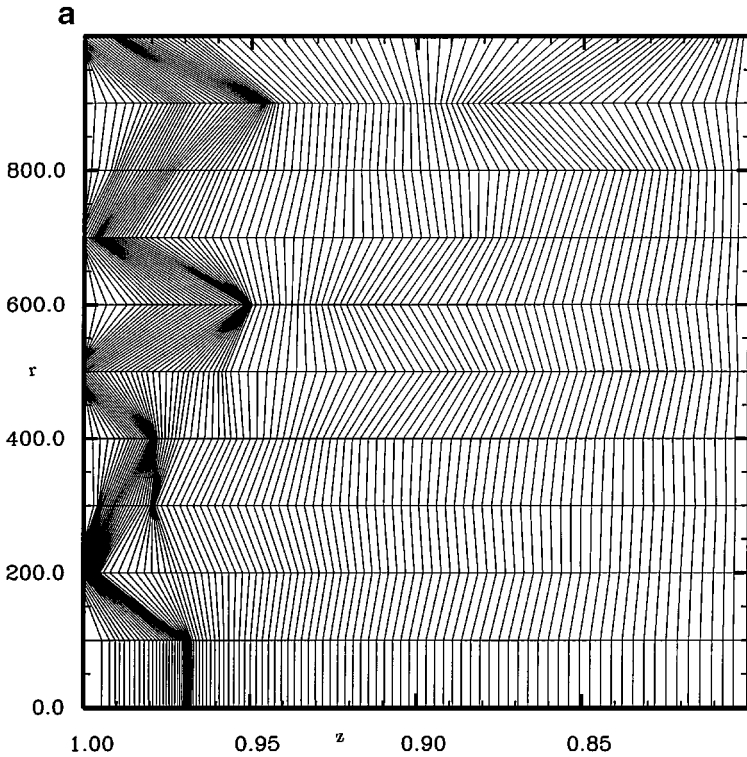


FIG. 12. (a) Saltzman piston problem: grid at time $t = 0.8$, aspect ratio of $10^4 \times 1$, merit factor = 0.0. (b) Saltzman piston problem: grid at time $t = 0.8$, aspect ratio of $10^4 \times 1$, merit factor = 1.0. (c) Saltzman piston problem: grid at time $t = 0.8$, aspect ratio of $10^4 \times 1$, merit factor = 2.0.

ratio using trigonometric functions that will cover very large fractions of the solution space. When such problems are run the same behavior is seen: large grid distortion and tangling without subzonal forces, and coherent, much-improved results with such forces and a merit factor in the range from one to three. However, the Saltzman problem, owing to its straight line initial grid, can be run at unit aspect ratio while the others cannot, and will always result in a grid that binds. Thus, the problem we address here is not one of excessive grid curvature, but of a grid slightly canted with respect to the physical solution. Grid distortion increases with a constant angular perturbation across a zone as the aspect ratio of that zone increases. The merit factor that we introduced was calibrated using this problem. That is, we see the same effect with subzonal forces from Eq. (14) using triangles as we do from Eq. (18) with subquadrilaterals if we multiply the subzonal forces of the latter by a factor of two. Using subquadrilateral forces differenced with Eq. (16) gives a weaker effect by about another factor of two or more because of the averaging done by these force contours when applied to this problem.

With regard to the form of the artificial viscosity used in the above example, we see from Fig. 12a that artificial viscosity alone was not effective in producing good results for this long-thin zone problem. However, the edge-centered viscosity used here [9] is generally better for long-thin zone problems than a zone-centered form. This is because the motions of the edges of a zone can be roughly uncorrelated if the zone is long and thin. In this instance a zone-centered artificial viscosity will generally respond to a shock wave impacting upon

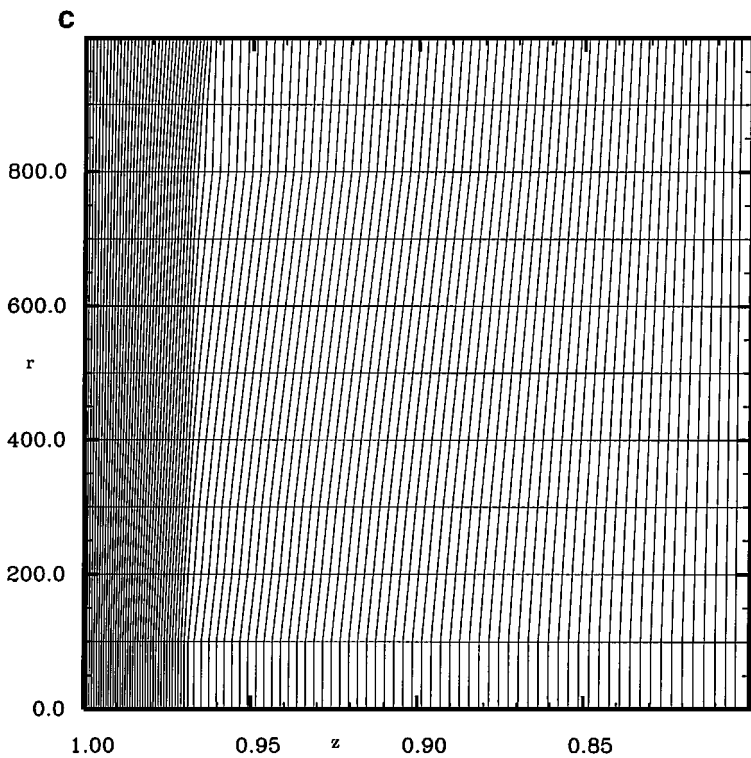
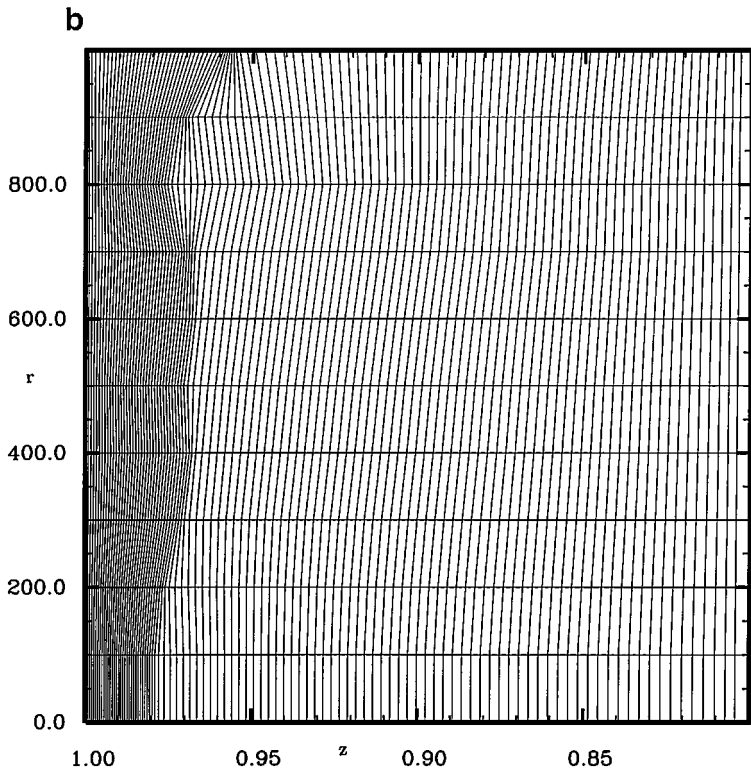


FIG. 12—Continued

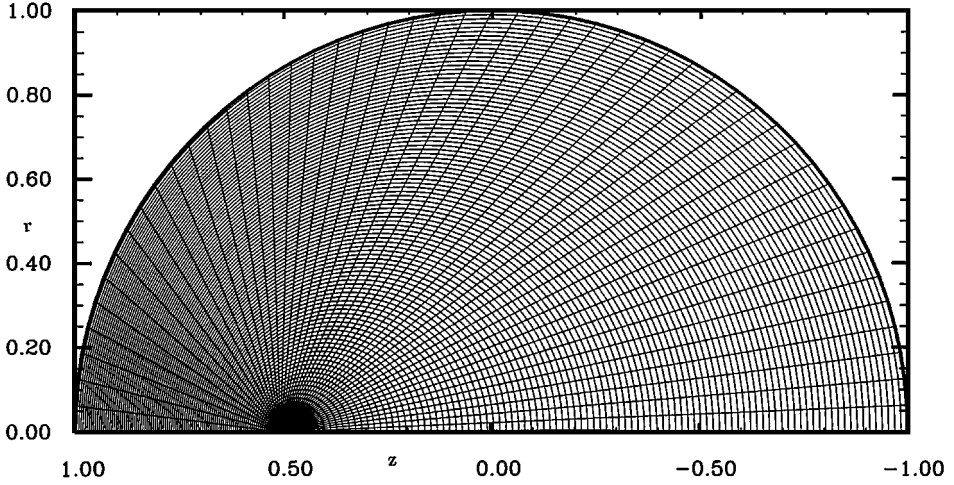
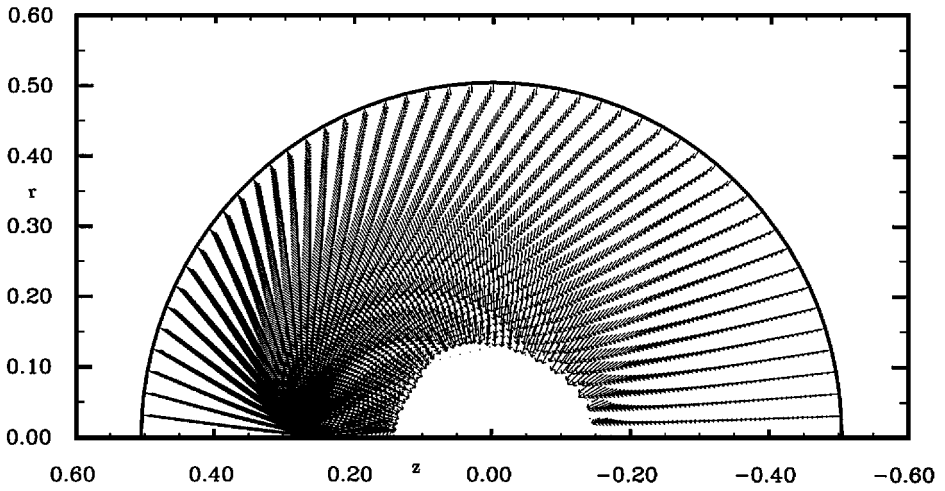
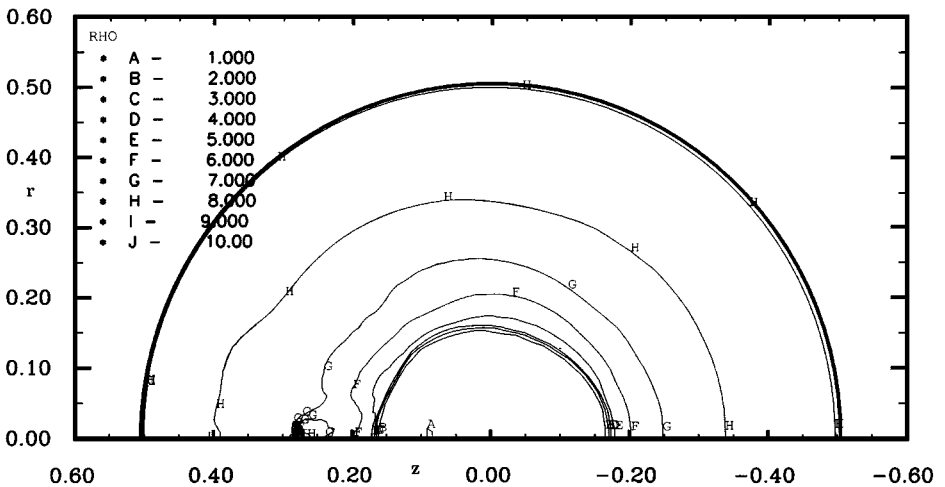
any portion of the zone, instead of just that of an individual edge, and can lead to unwanted spurious motion of the zone as a whole. We conclude from these results that an artificial viscosity should only be used to resolve shock wave disturbances and not to, in addition, control spurious zone distortion; for the latter purpose artificial viscosity will often be found to cause more harm than good.

Finally, the implosion problem of Lazarus [22] is run in cylindrical geometry using the initial grid shown in Fig. 13a. In this problem a sphere of unit radius, unit density, and zero internal energy initially, is driven by an inward radial velocity at the boundary with a time dependence that is calculated from a self-similar solution expressed as the answer to an ODE problem [22]. An approximate form for this expression as well as the solution for the density at our final time $t = 0.8$ is given in [17]. Our initial grid consists of 51 radial lines at equal angles on a 180° grid, and 101 circular lines with centers displaced so that the innermost circle lies at a false center of convergence that is 50% removed in radius from the center point of the outermost circle. It is this outermost circle that is driven with the velocity boundary condition that is centered on the point $(0., 0.)$. The false center of convergence is allowed to move with a velocity that is an average of that of points which lie initially on the circle next to it. This problem setup gives an extreme example of the general case where a center of convergence is not known in advance. The results shown are performed with an area-weight scheme [13, 17] using subzonal forces with a merit factor of 1.0.

The velocity vectors at the grid points and a contour plot of the density are given at time $t = 0.7$ in Figs. 13b, 13c. At this time the shock has moved past the false center of convergence and, from the velocity vectors, is headed for convergence at about the proper point $(0., 0.)$. The density contour shows a small perturbation about this false center, but the contours are still mostly circular. The shock wave converges at a point on the z -axis just after $t = 0.75$; this point is slightly to the left of $(0., 0.)$ showing that the false center of convergence has slowed the shock wave down slightly. This can be clearly seen in Figs. 13d, 13e where we show the grid and a contour plot of the density at $t = 0.8$ after the shock has reflected off the z -axis and is moving outward. Again, there is a small density perturbation at the false center of convergence. If this problem is run with this grid setup and without subzonal forces, the code will grid tangle and quit just as the shock wave intersects the false convergence center. A density contour plot for the same problem with identical run parameters but using an initial grid that has all circles centered at point $(0., 0.)$ is shown at time $t = 0.8$ in Fig. 13f for comparison. This result is very close to the known solution [17] and preserves spherical symmetry to roundoff error. If the symmetric problem whose result is given by Fig. 13f is run without subzonal pressure forces the resulting density profile will be virtually identical to that seen in this figure. The densities differ mostly in the fourth significant digit indicating that the subzonal pressure effects are at truncation error levels.

The point of this last comparison is that subzonal pressure forces remain at truncation error levels for problems that have shock discontinuities but not strong differential grid

FIG. 13. (a) Lazarus implosion problem: initial grid showing false center of convergence. (b) Lazarus implosion problem: grid point velocity vectors at time $t = 0.7$. (c) Lazarus implosion problem: contours of density at time $t = 0.7$. (d) Lazarus implosion problem: grid at time $t = 0.8$. (e) Lazarus implosion problem: contours of density at time $t = 0.8$. (f) Lazarus implosion problem: contours of density at time $t = 0.8$ using an initial grid with all circles centered at point $(0., 0.)$.

a**b****c**

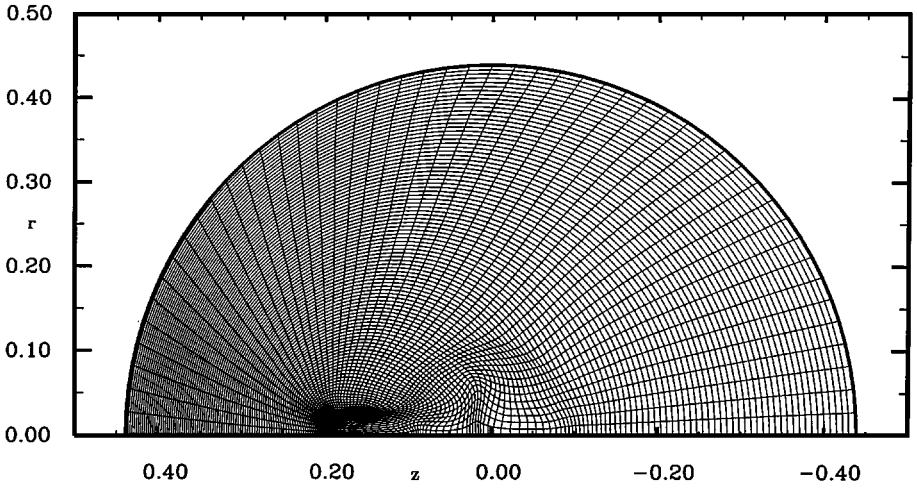
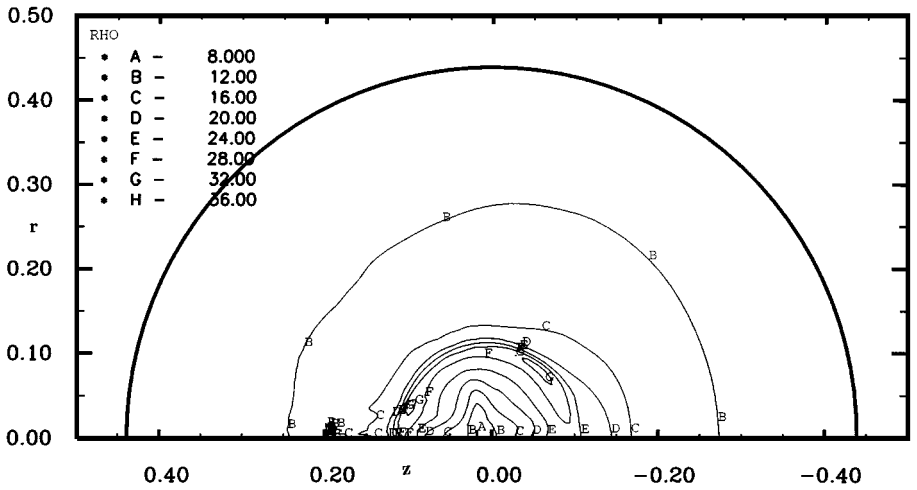
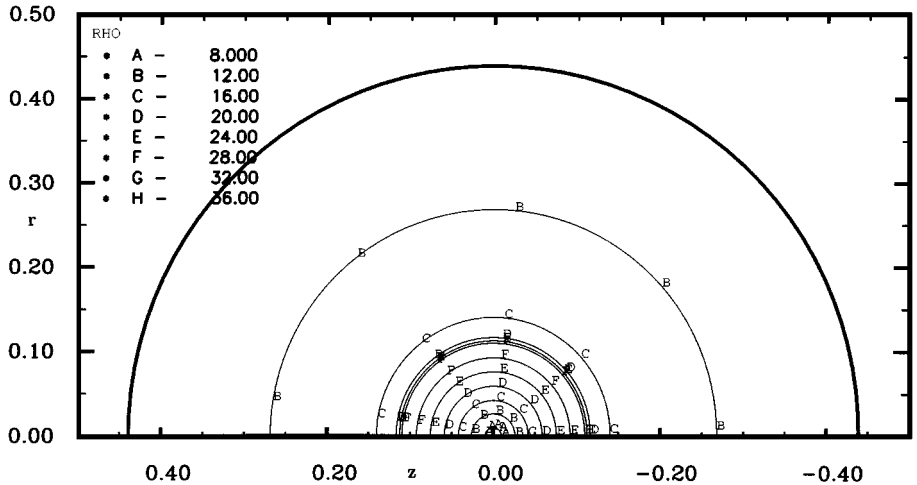
d**e****f**

FIG. 13—Continued

distortions. For these cases the differences caused by these forces are no larger than those that are seen due to truncation error when the spatial grid is refined by a factor of two. It is only when differential disturbances at the grid scale lengths occur that these forces become large. This is a kind of selective correction that prevents the introduction of spatial scales that the Lagrangian grid following the fluid motion cannot adjust to and resolve. These kind of short spatial scales result in grid tangling whether they originate from hourglass distortions on initially unit aspect ratio grids, as seen in the bending beam example, or from short scale distortions perpendicular to the main fluid flow as can occur for grids that have long-thin zones, as seen in the Saltzman piston problem run with very high aspect ratio initial zoning. In instances when the fluid flow is such that the Lagrangian assumption of a constant mass inside a given zone breaks down (for example, the beginning of turbulence) then the grid still does not tangle but effectively binds, becoming very thin in one direction with a consequent crash of the timestep resulting in run termination. This can be viewed as a form of artificial grid stiffening, but one that results from the fundamental assumption of a constant zonal mass being violated. The onset of this difficulty can be detected by progressively increasing values of $\delta\rho/\rho_z$ in time by an adjacent series of zones. This should result in an effective automated criterion for when to either split these zones, introducing additional dynamical points, or indicate how to move these points and flux in an effective ALE scheme. This is a subject for future work.

What we wish to stress is that a large value of the merit factor in a given run does not mean that subzonal forces are large in any sense compared to mean pressure forces. Likewise, a small value of the merit factor also does not mean that subzonal forces are small; they can be zeroth order no matter how the merit factor is reduced in the case where the onset of turbulence is being approached. This all depends on the nature of the fluid flow. The important result is that the unphysical, or spurious, part of the velocity field is always counteracted. In all of these problems we have looked to see how large the subzonal perturbed corner pressures become relative to the mean zone pressure. In most cases and over most of the grid this ratio is small, corresponding to what is expected from spatial truncation error. In problem regions of a calculation where the grid is trying to tear, this value can become much higher, ultimately to the point where it is zeroth order locally in order to prevent zone inversion. This occurs independently of the size of the merit factor, since the zone will simply distort a little more to make up for a smaller merit factor before grid inversion is prevented. For example, in the very high aspect ratio Saltzman piston problem a very few zones along the shock front have values of perturbed corner pressure that are 20% or more of the mean zone pressure.

Finally, we address the increased overhead associated with this algorithm. First, one must compute the volumes of the subzones in order to derive the subzonal densities. Depending on how one chooses to code the forces that result from the mean pressures the coordinate-line mesh may not need to be computed if subzonal forces are omitted, but for other instances where preservation of certain symmetries is important this is still needed anyhow [17]. The maximum of the perturbed corner pressure in a zone is added to the mean zone pressure and used to derive an effective zone sound speed from which the timestep is computed from the usual CFL condition; however, the scale lengths used in computing this condition are still those of the entire zone and not those of the subzone volumes [13] so that the timestep is not really decreased much over that obtained without the subzonal pressures. The artificial viscosity and material strength forces are unchanged. In the results presented here we require five calls to the equation of state for each zone, since we need the pressure in each

subquad from which we subtract the zone mean pressure to obtain δp . For most equations of state a good approximation to δp can be simply obtained by setting $\delta p = c_s^2(\delta\rho)$, where c_s is the mean speed of sound in the zone and $\delta\rho$ is the difference between the subzone and zone densities; this has been tried and works well. A bit of variation in this quantity does not matter since, as has been discussed, there is not a strong sensitivity to the values of the merit factor, which can be allowed to vary from one zone to another. Thus, although this extra overhead will depend somewhat on the choices one makes in implementation, generally it will be rather small, on the order of 10% to 20% on a pure hydro timestep.

8. CONCLUSIONS

In this paper we have investigated the problem of anomalous grid distortion in Lagrangian algorithms that arise both from unresolved, high spatial frequency hourglass-type motions, and spurious grid vorticity generation that occurs at somewhat larger spatial grid scales. The extension of the Lagrangian assumption to include both the zonal and nodal mass, as well as subzonal masses as the intersection of zone and node Lagrangian boundaries led to the introduction of subzonal densities and pressures. This result gave rise to nondynamical points whose force contributions must be distributed to the dynamical points in some momentum conserving manner. It is the subzonal forces associated with these pressures that stabilize the Lagrangian grid with respect to spurious distortions. However, the manner in which these forces could be distributed to the dynamical points is nonunique, essentially because the force now depends on the integration path taken through a given zone. This led us to treat the subzonal forces as perturbations distinct from the mean pressure forces of the zone, and to introduce a zone dependent “merit factor” that multiplies the magnitude of these forces. In the numerical examples it was shown that although this merit factor could often be set to unity it was sometimes efficacious to make it larger or smaller than this value; it can also be easily automated based on the magnitude of subzonal density variation.

The procedure developed here is extremely simple to implement into existing codes. Although we have cast our development in the framework of compatible discretizations, this need be done only for the subzonal force modification. In this case it is enough to first choose a form for the perturbed corner force $\delta\mathbf{f}_z^p$, say Eq. (18), that must be appropriately computed and then summed about the dynamical points to obtain the total perturbed force, $\delta\mathbf{F}_p$, that is employed in the momentum equation, Eq. (6). Finally, the work done by these forces must be computed compatibly using the internal energy equation as given by Eq. (7). However, this last operation can be performed separately from the rest of the internal energy update. Thus, the entire algorithm need not be in compatible form, although this is the differencing that we recommend.

The main result of this work is to extend Lagrangian hydrocodes to the limit where the assumption of a Lagrangian zonal mass breaks down, rather than have them quit prematurely due to purely spurious numerical difficulties. The numerical results were aimed at showing that this has been achieved with a number of examples whose solutions are either known analytically or well documented numerically, for both high-speed and low-speed flow problems. While a properly constructed artificial viscosity can afford some mitigation of spurious grid distortion it was shown that the method presented here is much superior, while being nondissipative. The intention is that this work can be combined with advection

schemes when needed, as part of an ALE or other advective formulation, to simulate a very wide range of fluid flow problems.

ACKNOWLEDGMENTS

We thank D. Burton, L. Margolin, and P. Whalen for stimulating discussions. This work has been supported under the auspices of the ASCI initiative.

REFERENCES

1. *Fundamental Methods in Hydrodynamics*, edited by B. Alder, S. Fernback, and M. Rotenberg, Methods in Computational Physics (1964), Vol. 3.
2. G. Maenchen and S. Sack, *The Tensor Code*, Methods in Computational Physics (1964), Vol. 3, p. 181.
3. L. G. Margolin and J. J. Pyun, A method for treating hourglass patterns, in *Proc., Numerical Methods in Laminar and Turbulent Flow*, edited by C. T. Taylor and N. M. Hafey (1987), p. 149.
4. D. P. Flanagan and T. Belytschko, A uniform strain hexahedron and quadrilateral with orthogonal hourglass control, *Int. J. Numer. Methods Eng.* **17**, 679 (1981).
5. J. K. Dukowicz and B. Meltz, Vorticity errors in multidimensional Lagrangian codes, *J. Comput. Phys.* **99**, 115 (1992).
6. P. L. Browne and K. B. Wallick, *The Reduction of Mesh Tangling in Two-Dimensional Lagrangian Hydrodynamics Codes by the Use of Viscosity, Artificial Viscosity, and Temporary Triangular Subzoning (TTS) for Long-Thin Zones*, Los Alamos Laboratory Report, LA-4740-MS, 1971.
7. W. D. Schulz, *Two-Dimensional Lagrangian Hydrodynamic Difference Schemes*, Methods in Computational Physics (1964), Vol. 3, p. 1.
8. W. D. Schulz, unpublished notes, 1979.
9. E. J. Caramana, M. Shashkov, and P. P. Whalen, An edge-centered artificial viscosity for multi-dimensional shock wave computations, *J. Comput. Phys.*, in press.
10. D. E. Burton, private communication.
11. V. M. Goloviznin, R. A. Volkova, and V. K. Korshunov, Two-dimension variational difference schemes of gas dynamics with a multiplet number of thermodynamic degrees of freedom, preprint No. **64**, M. V. Keldysh Institute of Applied Mathematics, Moscow, Russia, 1982.
12. D. E. Burton, *Conservation of Energy, Momentum, and Angular Momentum in Lagrangian Staggered-Grid Hydrodynamics*, Lawrence Livermore National Laboratory Report, UCRL-JC-105926, 1990.
13. E. J. Caramana, D. Burton, M. Shashkov, and P. P. Whalen, The development of compatible, mimetic, hydrodynamics algorithms utilizing conservation of total energy, *J. Comput. Phys.*, in press.
14. A. A. Samarskii, V. F. Tishkin, A. P. Favorskii, and M. J. Shashkov, Operational finite difference schemes, *Differential Equations* **17**, 854 (1981).
15. M. Shashkov, *Conservative Finite-Difference Methods on General Grids* (CRC Press, Boca Raton, FL, 1996).
16. C. Hirsch, *Numerical Computation of Internal and External Flows* (Wiley-Interscience, New York, 1991), Vol. 1.
17. E. J. Caramana and P. P. Whalen, Numerical preservation of symmetry properties of continuum problems, *J. Comput. Phys.* **141**, 174 (1998).
18. M. J. Fritts and J. P. Boris, The Lagrangian solution of transient problems in hydrodynamics using a triangular mesh, *J. Comput. Phys.* **31**, 173 (1979).
19. S. R. Orr, private communication.
20. F. H. Harlow and A. A. Amsden, *Fluid Dynamics*, LASL Monograph, LA-4700, June 1971.
21. J. Saltzman and P. Colella, *Second Order Upwind Transport Methods for Lagrangian Hydrodynamics*, LAUR-85-678, Los Alamos National Laboratory Report, 1985.
22. R. Lazarus, Self-similar solutions for converging shocks and collapsing cavities, *SIAM J. Numer. Anal.* **18**, 316 (1981).